

1 **Revision 1**

2
3 **Volcanic SiO₂-Cristobalite: A natural product of Chemical Vapor**
4 **Deposition**

5
6 C. Ian Schipper^{1*}, William D.A. Rickard², Steven M. Reddy^{2,3}, David W. Saxey², Jonathan
7 M. Castro⁴, Denis Fougerouse², Zakaria Quadir², Chris Conway⁵, David J. Prior⁶, Kat Lilly⁶
8

9 ¹ School of Geography, Environment and Earth Sciences, Victoria University, PO Box 600,
10 Wellington 6140, New Zealand

11 ² John de Laeter Centre, Curtin University, GPO Box U1987, Perth, WA 6845, Australia.

12 ³ School of Earth and Planetary Sciences, Curtin University, , GPO Box U1987, Perth, WA
13 6845, Australia.

14 ⁴ Institute for Geosciences, Johannes Gutenberg University, Mainz, Germany, 55099

15 ⁵ Geological Survey of Japan, AIST, 1-1-1 Higashi, Tsukuba, Ibaraki 305-8567, Japan

16 ⁶ Geology Department, University of Otago, PO Box 56, Leith St., Dunedin 9016, New
17 Zealand

18
19 *ian.schipper@vuw.ac.nz
20

21 **Abstract**

22 Cristobalite is a low-pressure, high-temperature SiO₂ polymorph that occurs as a metastable
23 phase in many geologic settings, including as crystals deposited from vapor within the pores
24 of volcanic rocks. Such vapor-phase cristobalite (VPC) has been inferred to result from
25 silica redistribution by acidic volcanic gases (e.g., HF), but a precise mechanism for its
26 formation has not been established. We address this by investigating the composition and
27 structure of VPC deposited on plagioclase substrates within a rhyolite lava flow, at the
28 micrometer to nanometer scale. The VPC contains impurities of the form [AlO₄/Na⁺]⁰ –
29 coupled substitution of Al³⁺ charge-balanced by interstitial Na⁺ – which are typical of
30 cristobalite. However, new EPMA element maps show individual crystals to have impurity
31 concentrations that systematically decline from crystal cores-to-rims, and atom probe
32 tomography reveals localized segregation of impurities to dislocations. Impurity
33 concentrations are inversely correlated with degrees of crystallinity (observed by EBSD,
34 hyperspectral CL, Laser Raman, and TEM), such that crystal cores are poorly crystalline and
35 rims are highly ordered tetragonal α -cristobalite. The VPC-plagioclase interfaces show

36 evidence that dissolution-precipitation reactions between acidic gases and plagioclase
37 crystals yield precursory amorphous SiO₂ coatings that are suitable substrates for initial
38 deposition of impure cristobalite. Successive layers of cubic β-cristobalite are deposited with
39 impurity concentrations that decline as Al-bearing gases rapidly become unstable in the
40 vapor cooling within pores. Final cooling to ambient temperature causes a displacive
41 transformation from β→α cristobalite, but with locally expanded unit cells where impurities
42 are abundant. We interpret this mechanism of VPC deposition to be a natural proxy for
43 dopant-modulated Chemical Vapor Deposition, where halogen-rich acidic gases uptake
44 silica, react with plagioclase surfaces to form suitable substrates, and then deposit SiO₂ as
45 impure cristobalite. Our results have implications for volcanic hazards, as it has been
46 established that the toxicity of crystalline silica is positively correlated with its purity.
47 Furthermore, we note that VPC commonly goes unreported, but has been observed in silicic
48 lavas of virtually all compositions and eruptive settings. We therefore suggest that despite
49 being metastable at Earth's surface, cristobalite may be the most widely occurring SiO₂
50 polymorph in extrusive volcanic rocks and a useful indicator of gas-solid reaction having
51 occurred in cooling magma bodies.

52

53

Introduction

54 Quartz is the nominally stable and most abundant silica (SiO₂) polymorph in Earth's
55 crust (Fig. 1a), but is typically found only in the most silicic of volcanic rocks (Bowen 1928,
56 Gualda and Ghiorso 2013). Conversely, the low-pressure, high-temperature SiO₂
57 polymorph cristobalite can be found in lava flows and domes with compositions ranging
58 from basaltic (e.g., Van Valkenburg and Buie 1945) to rhyolitic (e.g., Swanson et al. 1989).
59 Efforts to understand volcanic cristobalite have been driven by the concern that it can
60 exacerbate volcanic hazards, either by causing lung cancer or silicosis in people living near

61 active volcanoes (e.g., Baxter et al. 1999), or by sealing permeable pathways in volcanic
62 edifices and making them prone to explosive failure (e.g., Boudon et al. 2015). Furthermore,
63 cristobalite has been recognized as a useful indicator of low-pressure degassing processes
64 and gas-solid reactions in volcanic systems (e.g., Schipper et al. 2017).

65 Cristobalite is considered to be “metastable” when preserved at ambient
66 temperatures, because these are outside its nominal stability field within the pure SiO₂
67 system (<0.2 MPa, 1470-1727 °C; Heaney 1994) (Fig. 1a). However, cristobalite is common
68 at Earth’s surface and has high- and low-temperature metastable forms: cubic β-cristobalite
69 and tetragonal α-cristobalite, with the β→α displacive transition occurring at ~240 °C
70 (Horwell et al. 2013). It is often present as “stuffed derivatives,” with impurities
71 incorporated into its relatively open structure (Buerger 1954). These impurities are usually
72 of the form [AlO₄/M⁺]⁰, representing coupled substitution of Al³⁺ for Si⁴⁺ in Si-O tetrahedra,
73 charge-balanced by interstitial monovalent cations (M⁺ = Na⁺, K⁺, Li⁺, H⁺) (Smith and
74 Steele 1984). The presence of these impurities can prevent the reconstructive transformation
75 to quartz during cooling to ambient temperature (Deer et al. 1992, Heaney 1994), can
76 stabilize β- and α-forms outside their stability fields (e.g., Perrotta et al. 1989, Chao and Lu
77 2002), and can increase the size of unit cells and lower/broaden the temperature range of the
78 β→α transition (Damby et al. 2014).

79 Volcanic cristobalite forms both by devitrification and by deposition from a vapor
80 phase (Damby 2012, Horwell et al. 2013). Devitrification results in spherulites or altered
81 groundmass glass in lava bodies and shallow intrusions (Swanson et al. 1989, Horwell et al.
82 2013). Devitrification is not the focus of this work, but does contribute substantially to the
83 total crystalline SiO₂ content of many volcanic rocks. In lava samples with high (>10s of
84 wt%) bulk cristobalite contents, most can be attributed to devitrification (Damby 2012,
85 Schipper et al. 2015). Here, we focus on vapor-phase cristobalite (VPC), which occurs as

86 idiomorphic crystals grown within the pores or vesicles of volcanic rocks (Horwell et al.
87 2013) (Fig. 1b-e). It is common for a given cristobalite-bearing volcanic rock to contain both
88 devitrification and vapor-phase cristobalite. However, many VPC-bearing rocks retain
89 glassy groundmasses with no signs of devitrification, so these forms of volcanic cristobalite
90 are thought to form independently, but often concurrently (Schipper et al. 2015).

91

92 **A general mechanism for vapor-phase cristobalite formation**

93 The working qualitative mechanism for VPC formation relies on the reactivity of
94 acidic volcanic gases with aluminosilicate materials to explain VPC occurrences and
95 textures (Damby 2012, Schipper et al. 2017). As magma cools at low pressures, halogens
96 partition into aqueous fluids within pore networks to form acidic gas species (HF, HCl)
97 (Aiuppa et al. 2009, Schipper et al. 2019). These acidic gases can corrode/dissolve
98 aluminosilicate material around pores (Oelkers 2001, Wolff-Boenisch et al. 2004), taking up
99 silica and other elements into the vapor phase. Volatilized Si exists in the vapor in various
100 forms, including as halogen complexes (e.g., SiCl_4 , SiF_4 ; de Hoog et al. 2005, Horwell et al.
101 2013). Both chlorine and fluorine are suitable ligands for Si, but HF is significantly more
102 reactive than HCl. Unlike HCl, HF directly attacks Si-O bonds within aluminosilicate
103 frameworks, and is therefore more efficient at corroding glass, and thought to be crucial for
104 mobilizing SiO_2 (Schipper et al. 2017). Eventual deposition of SiO_2 as VPC is thought to
105 occur when the vapor phase has become saturated in silica.

106 This mechanism has not yet been experimentally proven, but does explain some key
107 features of VPC occurrence and textures within established paradigms of volcanic
108 degassing. Firstly, slowly-cooled magma bodies should have greater potential to produce
109 VPC because the halogens required for SiO_2 mobilization exsolve from magmas that are
110 emplaced at low-pressures in thermally-insulated flows or domes, rather than by

111 decompression during magma ascent (Aiuppa et al. 2009, Balcone-Boissard et al. 2010).
112 This is reflected in the inverse correlation between lava extrusion rates and (sometimes)
113 direct correlation between dome residence times and cristobalite contents of dome-derived
114 tephra (Horwell et al. 2014). It also explains why VPC is sometimes found in the slowly-
115 cooled effusive, but not the rapidly-quenched explosive, products of some volcanic
116 eruptions (Schipper et al. 2015). Secondly, VPC-bearing pores in volcanic rocks often retain
117 textural evidence of the corrosion process having occurred. Silicate minerals are more
118 corrosion resistant than co-existing aluminosilicate glasses (Oelkers 2001), so the acid
119 corrosion process rapidly removes glass from around pores, leaving behind identifiable
120 lattice networks of silicate minerals in corrosion rims (de Hoog et al. 2005, Damby 2012,
121 Schipper et al. 2015, Schipper et al. 2017) (Figs. 1-2). Thirdly, VPC has been found in
122 association with halogen-rich secondary minerals (e.g., F-phlogopite) further suggesting an
123 association with HF reactivity (de Hoog et al. 2005). The outstanding problem with the
124 corrosion-deposition model, is that it does not actually describe the deposition process of
125 cristobalite. Deposition of VPC is assumed to have occurred based on its existence, but this
126 remains the unexplained – and definitive – step in its formation.

127 To describe VPC formation as “vapor deposition” or “vapor mineralization” suggests
128 some proxy for the Chemical Vapor Deposition processes that are used in the industrial
129 manufacture of thin-film devices (e.g., Pierson 1999, Foggiate 2001). Interestingly,
130 industrial deposition of SiO₂ films often use Si-bearing source gases that are similar to those
131 emitted from volcanoes (e.g., SiCl₄ or SiF₄) (Klaus and George 2000, Nakahata et al. 2000).
132 However, these are not directly comparable to volcanic scenarios because industrial
133 Chemical Vapor Deposition is carried out with crystallographically appropriate substrates,
134 under optimised conditions (e.g., pressures and temperatures), and/or using catalysts: all of
135 which are chosen by engineers rather than dictated by nature. Still, there are fundamental

161 slowly-cooled core of the lava flow (Schipper et al. 2015). The lava contains both
162 devitrification and vapor-phase cristobalite, with the former being more abundant. We
163 investigate individual VPC crystals from a selection of 33 Cordón Caulle lava samples
164 (Schipper et al. 2015, Schipper et al. 2019). The number of samples and individual VPC
165 crystals analyzed by each technique varied as the investigation proceeded.

166

167 **Analytical methods**

168 Whole VPC crystals from six different lava samples were observed by secondary
169 electron microscopy (SEM) on unpolished rock chips with open vesicles. Images were
170 collected with a JEOL 6610 SEM at Victoria University of Wellington, using 15 kV
171 accelerating voltage and 8 nA beam current. All 33 lava samples were investigated in thin
172 section using a flatbed scanner, petrographic microscope, and backscatter electron (BSE)
173 imaging. BSE images were collected with the JEOL JXA-8230 Superprobe at Victoria
174 University, using 15 kV accelerating voltage and 8 nA beam current. BSE imaging was used
175 to select individual VPC crystals for analysis, targeting those that appeared to be cut sub-
176 equatorially in the thin sectioning process. This ensured that analyses on a single polished
177 surface captured material that is representative of both crystal cores and rims.

178 Major element compositions of VPC crystals were determined by several different
179 applications of electron probe microanalysis (EPMA), using the JXA-8230 at Victoria
180 University. One approach was to use wavelength dispersive spot analyses along core-to-rim
181 transects across 23 different VPC crystals from seven different lava samples. Transects used
182 1 μm spot size, 15 kV accelerating voltage, beam currents ranging from 2 – 12 nA, and
183 peak/background counting times of 30/15 seconds. Another approach was to obtain EPMA
184 element maps of 51 VPC crystals from seven lava samples. Maps used a focused beam, 15
185 kV, 12 nA, 0.5 μm step size, and a short dwell time of only 400 ms. During mapping, only

186 Si, Al, Na, K and Ti were analyzed by wavelength dispersive spectroscopy, with a full suite
187 of elements simultaneously collected by energy dispersive spectroscopy. Additional semi-
188 quantitative analysis of more than 50 VPC crystals from ~20 samples was performed by
189 energy dispersive spot analysis during sample investigation.

190 Hyperspectral cathodoluminescence (CL) spectra were obtained concurrently with
191 EPMA maps, using a JEOL xCLent spectrometer installed in the optical pathway of the
192 JXA-8230. At each pixel in the maps, CL intensities across a wavelength range of 350-1000
193 nm (3.542 – 1.240 eV) were collected simultaneously and processed using the xCLent
194 Image software package.

195 Structure and orientation analysis of VPC crystals was carried out by electron
196 backscatter diffraction (EBSD) at the University of Otago (Dunedin, New Zealand) and
197 Curtin University (Perth, Australia). At Otago, EBSD patterns of 77 VPC crystals from four
198 lava samples were obtained with a Zeiss Sigma VP FEGSEM fitted with an Oxford
199 Instruments Nordlys camera. Crystals were analysed using 30 kV, 50 nA and a mapping step
200 size of 500 nm. At Curtin, EBSD was performed on 20 crystals from a single lava sample
201 using a Tescan MIRA VP-FEGSEM at 20 kV and ~1 nA, and step size of 200 nm. All
202 analyses were undertaken at 70° tilt. Data were acquired using the Aztec software package
203 version 3.3 and processed using Channel 5.12 software, both from Oxford Instruments.
204 Match units for cristobalite were based on crystallographic data of Downs and Palmer
205 (1994). EBSD map files were noise reduced using widspike and 5-nearest-neighbour zero
206 solution protocols.

207 Laser Raman analysis of 15 VPC crystals from five lava samples was performed
208 using a Horiba JY LabRam HR800 at Victoria University. Raman analysis was performed
209 in the backscattering configuration, with a 633-nm He-Ne laser for excitation, a holographic
210 notch filter, a 600 mm⁻¹ grating, and a liquid-nitrogen cooled CCD detector. The laser power

211 at the sample was 5 mW. Light was delivered and collected through an Olympus microscope
212 objective with $\times 100$ magnification (focal length 1.8 mm, NA 0.9), resulting in a probed area
213 on the sample surface of approximately 1 μm diameter. The spectral resolution was on the
214 order of 3 cm^{-1} , and spectra were integrated over a 10 s acquisition time.

215 Site specific samples for nanoscale compositional and structural analysis were
216 extracted from areas of interest within VPC crystals using a Tescan Lyra3 Focused Ion
217 Beam (FIB) SEM at Curtin University. The FIB-SEM used a Ga^+ ion source and Pt
218 deposition was used as a protective layer during high current milling.

219 Twenty needle shaped specimens from three VPC crystals were prepared for atom
220 probe tomography (APT). These had lengths of $\sim 2\text{ }\mu\text{m}$ and tip diameters of $\sim 100\text{ nm}$, and
221 were extracted and mounted on prefabricated Si micro-tip coupons. Ion-beam milling of
222 APT specimens was carried out at 30kV with a final low-kV (2kV) milling step being used
223 to minimise beam damage and Ga implantation. Trace and major element distributions at the
224 nanoscale were investigated in 3D using the Cameca local electrode atom probe (LEAP)
225 4000X HR housed at the Geoscience Atom Probe facility at Curtin University, Australia.
226 Atom probe data were manually ranged and reconstructed within Cameca's IVAS 3.8
227 software. Elemental abundances and spatial distributions in each specimen were also
228 calculated with this software package.

229 A total of six foils from two VPC crystals were prepared for transmission electron
230 microscopy (TEM). These were mounted onto a copper grid and thinned to 100 nm by FIB
231 milling. TEM analysis was performed on an FEI Talos FS200X G2 TEM/scanning TEM
232 (STEM) microscope operated at 200 kV and equipped with a Super-X EDS system located
233 at Curtin University.

234

235

236

237

Results

238 **Textures**

239 The cristobalite crystals on which we focus here are identical to those that have
240 previously been described in the literature as the products of vapor-phase mineralisation
241 (Damby 2012, Horwell et al. 2013, Schipper et al. 2015). VPC is idiomorphic, which is
242 typical for crystals having grown from a vapor, unconstrained by surrounding melt (Fig. 1b).
243 The VPC host vesicles have typical corrosion rims (Fig. 1c), consisting of a lattice network
244 of microlites, but free of interstitial glass (Damby 2012, Schipper et al. 2015). Crystals can
245 approach ~100 μm in size, and usually have the characteristic “fish scale” cracking that is
246 attributed to a volume reduction experienced during the ~240 °C displacive β (cubic) \rightarrow α
247 (tetragonal) transition (Horwell et al. 2013) (Fig. 1d-e).

248 Our examination of VPC crystals in thin section shows them all to have contact with-
249 or attachment to- one or more plagioclase crystal(s) at their bases. The specific plagioclase
250 crystal(s) to which each VPC crystal is attached can be difficult to identify when VPC has
251 grown onto a polycrystalline lattice of microlites (Fig. 1d). However, in rare cases where
252 large plagioclase phenocrysts intersect pores, the attachment of VPC directly to plagioclase
253 is clear (Fig. 1e).

254

255 **Major element composition**

256 The results of EPMA spot analysis on Cordón Caulle VPC are summarized in Table
257 1, expressed by convention as element oxides. The VPC contains between 93.6 – 99.6 wt%
258 SiO_2 . The most abundant “impurities” (e.g., non- SiO_2 components) are Al_2O_3 (0.19 – 4.17
259 wt%) and Na_2O (0 – 4.7 wt%). The other major oxides that are common in silicate minerals
260 (K_2O , TiO_2 , CaO , MgO , FeO , P_2O_5) were only measured in one crystal, and in only trace

261 amounts (< 0.1 wt%) (Table 1). These results are similar to those of several other studies on
262 volcanic cristobalite (Damby 2012, Horwell et al. 2012, Damby et al. 2013, Schipper et al.
263 2015, Schipper et al. 2017). They suggest that impurity cations are of the expected co-
264 substitutional $[\text{AlO}_4/\text{M}^+]^0$ form (Buerger 1954), with sodium being the dominant interstitial
265 monovalent cation ($\text{M}^+ = \text{Na}^+$). However, we found sodium to be highly mobile under
266 electron beam irradiation, and many of the spot analyses in this study (and previous studies
267 by our group; Schipper et al. 2015, Schipper et al. 2017) are thought to have altered the
268 initial Na_2O concentrations (see below for further notes on beam damage). Potassium
269 concentrations in VPC are low, despite $[\text{AlO}_4/\text{K}^+]^0$ being common in the SiO_2 polymorph
270 tridymite, which is also found in many volcanic rocks (Kayama et al. 2009) but has not been
271 found at Cordón Caulle. It is possible that the VPC also contains trace amounts of other
272 monovalent cations (e.g., Li^+ or H^+ ; Smith and Steele 1984), but these were not detected by
273 EPMA analysis.

274 Compositional EPMA maps show impurities to systematically decline in
275 concentration from crystal cores (at pore walls) to rims (Fig. 2). Similar core-to-rim
276 increases in SiO_2 and decreases in Al_2O_3 and Na_2O were seen in all equatorially cut Cordón
277 Caulle VPC crystals, and were semi-quantitatively identified in >50 other VPC crystals from
278 Cordón Caulle (and Mt Ruapehu) by energy dispersive spot analysis. The short dwell time
279 used in the EMPA mapping routine appears to have prevented or diminished the problem of
280 Na migration that was encountered with EPMA spot analyses. It is by convention that the
281 major elements are expressed as oxides, but when cast as cation moles along core-to-rim
282 transects (Fig. 2e), it is apparent that the $\text{Al}^{3+}/\text{Na}^+$ ratio is ~ 1 across a wide range of
283 concentrations, as expected for co-substitutional $[\text{AlO}_4/\text{Na}^+]^0$ impurities (Smith and Steele,
284 1984).

285

286

287 **Micrometer-scale crystal structure**

288 Electron backscatter diffraction was used to identify VPC crystals and study their
289 microstructure. Cordón Cauille VPC exhibited very dramatic band contrast variation within
290 crystals (Fig. 3a), which is a measure of the quality of the diffraction patterns during EBSD
291 analysis (Prior et al. 2009). Crystal cores show weaker diffraction than crystal rims.
292 Accordingly, indexing is poor in crystal cores, whereas crystal rims readily and exclusively
293 index as tetragonal α -cristobalite (Fig. 3b). Domain boundaries are dominantly parallel to
294 $\{101\}_\alpha$, with others parallel to $\{112\}_\alpha$ (Fig. 3c). These (as well as the crystal cracking seen
295 in BSE images) are consistent with the Cordón Cauille VPC having undergone a $\beta \rightarrow \alpha$
296 transition. Boundaries parallel to $\{101\}_\alpha$ and $\{112\}_\alpha$ represent stacking faults inherited from
297 dislocations on $\{111\}_\beta$, and twins generated from reflection across $\{101\}_\beta$, respectively
298 (Christie et al. 1971).

299 Cathodoluminescence in silica polymorphs can arise from many different types of
300 defects and/or incorporation of different impurities, some of which are still poorly
301 constrained (Stevens-Kalceff et al. 2000). Hyperspectral CL maps of Cordón Cauille VPC
302 also show core-to-rim variation (Fig. 3d). Crystals have negligible luminescence (at any
303 wavelength) in crystal cores but strong luminescence in crystal rims, with a peak at ~ 2.7 eV
304 (459 nm) that is intrinsic to cristobalite (Moore and Karakus 1994).

305 Laser Raman spectra from crystal cores are featureless, while those from crystal rims
306 have peaks at ~ 230 and ~ 417 cm^{-1} . These vibrations are diagnostic of α -cristobalite (Kingma
307 and Hemley 1994) (Fig. 3e).

308 Cristobalite is known to be susceptible to beam damage under electron radiation,
309 particularly when it is impure (Christie et al. 1971, Chao and Lu 2002,). Some analytical
310 experimentation was required to determine the optimal way to capture all compositional and

311 structural trends within VPC. In the examples shown in Figures 2-3, Crystal L10-01 was
312 analysed first by EPMA spot analysis at 12 nA and then at 2 nA, and was then repolished
313 before analysis by EPMA mapping. Spot analyses yielded similar results in all elements
314 except Na₂O (results not shown but included in Table 1 summary), which was very low
315 regardless of current, but substantial in EPMA maps (Fig. 2d). Despite re-polishing before
316 subsequent analysis, 20 kV EBSD maps of Crystal L10-01 have tracks of obvious beam
317 damage where spot analysis transects were performed and this crystal has completely
318 unresolvable diffraction patterns in its core (Fig. 3). Conversely, Crystal L10-07 was
319 analysed first by 20 kV EBSD, and then by EPMA mapping. It still shows poor – but not
320 completely unresolvable – diffraction pattern strength in its core, which is rich in Al₂O₃ and
321 Na₂O. Initial EBSD tests using higher accelerating voltages of 30 kV (at U. of Otago)
322 resulted in significantly damaged crystals, in which Al₂O₃ concentrations were preserved but
323 Na₂O was almost completely lost. It appears that Na₂O is indeed highly mobile under
324 electron radiation, and that cristobalite structure degrades during this process. However,
325 EPMA and CL map data were collected simultaneously for all samples, and radial core-to-
326 rim patterns of decreasing [AlO₄/M⁺]⁰ and increasingly crystalline structure were observed
327 in all the analysed crystals. No detectable loss of Al₂O₃ was apparent in any analyses, which
328 is consistent with the Al³⁺ being substituted for Si⁴⁺ in the SiO₂ structure, rather than sitting
329 in interstitial lattice sites. An additional analytical note is that regular core-to-rim variation
330 in [AlO₄/Na⁺]⁰ and the resulting structures will only be apparent if analysing VPC crystals
331 that are cut sub-equatorially to their growth axes.

332

333 **Atomic-scale distribution of impurities**

334 The tendency for impurities to segregate to nanometer-scale discolations and other
335 such features has been shown analytically and computationally in a variety of geological

336 materials (e.g., Liu et al. 2016, Reddy et al. 2016), warranting an investigation of VPC at
337 these scales by atom probe tomography. Two specimen tips from the core and four tips from
338 the rim of one crystal yielded good results by APT, with $> 6 \times 10^6$ atoms detected (Table 2;
339 Fig. 4a). The mass-to-charge ratio spectrum of cristobalite is relatively simple compared to
340 other silicates (Fig. 4b). Silicon is present mainly as Si^+ , Si^{++} , Si^{+++} , SiO^+ , SiO^{++} , SiO_2^+ and
341 SiO_2^{++} . Aluminium was identified as Al^+ , Al^{++} , Al^{+++} , AlO^+ and AlO^{++} , while sodium was
342 present as Na^+ .

343 Bulk compositions of APT tips indicate the expected lower concentrations of Si and
344 higher concentrations of Al in the crystal core compared to the crystal rim (Table 2; Fig. 4e).
345 However, an unexpected result was that Na was below detection limit in specimens from the
346 core, and was in very low concentrations (<0.114 at%) in the rim. During data analysis,
347 ranging of Na is complicated by a peak overlap between Na^+ and SiO^{2+} at 23 Da, but this
348 should cause an overestimation of Na concentrations in Si-rich material. We suspect the low
349 Na concentrations to be the result of beam damage/Na loss that occurred prior to APT
350 analysis, which for this crystal included EBSD at 30 kV, EPMA spot and map analysis, and
351 FIB milling .

352 Tomographic reconstructions of APT data allow visualization of the spatial
353 distribution of atoms in 3D (Fig. 4c-d). Qualitatively, these show a heterogeneous
354 distribution of Al atoms in crystal cores, with short order clustering. All specimens from the
355 crystal rim appeared to have homogeneously distributed Al atoms, except for one (1361 in
356 Table 2) where a 7-10 nm wide linear feature containing high concentrations of Al atoms
357 was detected (Fig. 4d). Despite the apparent Na loss, comparison of Al concentrations from
358 APT analysis (Table 2) and along EPMA spot analysis transects from the same crystal (Fig.
359 4a,e) indicate similar Al for a given Si concentration throughout the crystal (expressed as
360 wt% oxides in Fig. 4e). Quantitative analysis of linear profiles using a small radius cylinder

361 through the core volumes reveal them in fact to have sawtooth concentration profiles with a
362 wavelength of 5-7 nm and magnitude of ± 0.3 at% Al (Fig. 4f). A linear concentration
363 profile taken across the Al-rich feature in the crystal rim revealed it to have almost twice as
364 much Al as seen anywhere in the crystal cores (Fig. 4f), despite the bulk Al concentration in
365 crystal rims being at all times significantly lower than that in crystal rims.

366

367 **Lattice structures within VPC and across the substrate-VPC interface**

368 Two Cordón Caulle VPC crystals were examined by Transmission Electron
369 Microscopy (TEM), using bright field and high resolution imaging. Diffraction patterns
370 were obtained using Fast Fourier Transform (FFT) analysis of high resolution TEM images.

371 The first crystal was the same one analyzed by APT (Fig. 4a), from which we used
372 TEM to examine foils lifted from the crystal core and rim (Fig. 5). Bright field images from
373 the crystal core show low-contrast lamellae that varied in width from 12-50 nm (Fig. 5a),
374 whereas images from the crystal rim had zones of mottled contrast and other zones of high-
375 contrast lamellae at a finer scale of 6-12 nm (Fig. 5b). The lamellae in the crystal core (Fig
376 5a) are similar to those that have been previously attributed to twin boundaries formed from
377 stacking faults in cristobalite (Christie et al. 1971, Withers et al. 1989a, Withers et al. 1989b,
378 Chao and Lu 2002). No lattice fringes were observed in high resolution images from regions
379 around the twin structures in the crystal core, which in itself would suggest the material to
380 be amorphous (Fig. 5c). However, FFT derived from these images (inset to Fig. 5c) have
381 diffuse rings, the inner one at 7.07 ± 0.08 Å, indicating that the VPC cores do contain some
382 degree of short-range order (e.g., Eckert et al. 2015). The high resolution images from the
383 crystal rims have distinct lattice fringes indicating a well-developed crystalline structure,
384 and the associated FFT have bright diffraction spots at 6.92 ± 0.02 Å (Fig. 5d). The
385 positions of the diffraction ring and spots in FFT from the core and rim are generally within

386 the ranges expected for $d(001)_\alpha$ (i.e., the c-axis) of tetragonal α -cristobalite (Deer et al.
387 1992). By assuming that distortion from an ideal tetragonal α -cristobalite structure will be
388 isotropic, the FFT data indicates the crystal core to have short-range order similar to α -
389 cristobalite but with an expanded $d(101)_\alpha$ of $4.12 \pm 0.05 \text{ \AA}$, and the rim to have $d(101)_\alpha$ of
390 $4.04 \pm 0.01 \text{ \AA}$. All TEM analysis had to be performed with minimal beam exposure times, as
391 rapid amorphization by the beam was apparent. This was particularly problematic in the
392 impurity-rich crystal cores, whereas the crystal rims were notably more resistant to beam
393 damage.

394 The other crystal investigated by TEM was selected because of it having a clearly-
395 identifiable plagioclase substrate crystal directly adjacent to the VPC core. This permitted a
396 TEM foil to be cut perpendicularly across the plagioclase-VPC interface (inset to Fig. 6).
397 High resolution TEM images across the interface show distinct lattice fringes in plagioclase
398 (confirmed by indexing of FFT, not shown). There is then an atomically sharp but slightly
399 undulating interface with a material that lacks any indication of structure except for some
400 slight mottled contrast, and appears similar to high resolution TEM images of VPC cores
401 (e.g., Fig. 5c). This amorphous material then meets a sharp interface with a slightly darker
402 but otherwise similar material. The interface between these two “amorphous” regions is at
403 an angle of $\sim 13^\circ$ to the plagioclase interface, so that the lighter one appears to be 36-43 nm
404 wide within the frame of the images (Fig. 6). The darker contrast in the second amorphous
405 layer could indicate that it has slightly higher density or slightly more short-range order than
406 the lighter amorphous layer. The sample was highly beam sensitive, and therefore, rapid
407 imaging was conducted to ensure the crystalline vs amorphous character of the core and rim
408 region.

409

410

Discussion

411 **Impurity distributions in vapor-phase cristobalite**

412 Natural cristobalite is usually impure, because it has a relatively open, low-pressure
413 SiO₂ framework into which cations can readily substitute (Buerger 1954). The ranges of
414 Al₂O₃ and Na₂O measured in Cordón Cauille VPC (Table 1, Fig. 2) are similar to those
415 reported in volcanic cristobalite from other locations (Damby 2012, Horwell et al. 2012,
416 Damby et al. 2013, Schipper et al. 2015, Schipper et al. 2017). Compositional heterogeneity
417 has been previously noted in volcanic cristobalite (Damby 2012), but systematic core-to-rim
418 variation has not been previously documented. The regular core-to-rim trend of decreasing
419 impurities in equatorially cut VPC crystals (Fig. 2) was observed in every VPC crystal we
420 investigated at Cordón Cauille, and also in VPC crystals from andesitic lava flows on Mt.
421 Ruapehu (e.g., as in Fig. 1e), suggesting that the core-to-rim impurity profiles are not unique
422 to select crystals, to Cordón Cauille, or to VPC in rhyolites.

423 The observed [AlO₄/Na⁺]⁰ profiles cannot be explained by cation diffusion into- or
424 out of- already-formed VPC. Aluminium diffusion rates in cristobalite are not specifically
425 known, but are very slow in other forms of SiO₂ (10⁻²⁴ m² s⁻¹ in quartz, Pankrath and Flörke
426 1994; 10⁻²² m² s⁻¹ in amorphous SiO₂, Francois-Saint-Cyr et al. 2003). Improbably long
427 times (many millenia) would therefore be required to develop the observed profiles by
428 diffusion. The profiles must therefore represent a temporal decline in [AlO₄/Na⁺]⁰
429 incorporation during SiO₂ deposition. From a purely bulk perspective, there should be no
430 shortage of Al³⁺ and Na⁺ available for incorporation into VPC. Compositional maps of the
431 groundmass around VPC-bearing pores in the Cordón Cauille lava flow by Schipper et al.
432 (2015) did not show any evidence for diffusive depletion of Al or Na from groundmass
433 glass. However, their work and the BSE images presented here show extensive evidence for
434 stoichiometric dissolution of glass from around pores (Fig. 1c). This should volatilize
435 substantial amounts of Al³⁺ and Na⁺ given that glass in the Cordón Cauille lava flow is rich

436 in these elements (>13 wt% Al₂O₃ and >3 wt% Na₂O; Castro et al. 2013, Schipper et al.
437 2019). With no limit on the availability of impurity cations, there must be some other
438 control on their incorporation into VPC.

439 The significance of the atomic-scale Al³⁺ concentration profiles observed in
440 impurity-rich VPC (Fig. 4f) is not clear, and to our knowledge no appropriate proxies for
441 cristobalite have been previously investigated by APT. Studies have used APT to
442 demonstrate that impurity clumping can be linked to crystal growth kinetics in some
443 minerals (e.g., Fougrouse et al. 2016, Wu et al. 2019), to document segregation of co-
444 substituted trace elements in others (Reddy et al. 2016), and have shown B³⁺ cations –
445 which are identical in charge but of much smaller ionic radius than Al³⁺ – to cluster in B-
446 doped silicon (Blavette et al. 2010, Raghuwanshi et al. 2015). Perhaps more directly
447 relevant to VPC are the similarly fine-scale chemical heterogeneities that have been
448 documented in synthetically Al/Na-doped cristobalite (Chao and Lu 2002), and the
449 calculated geometric optimization studies that have shown Al³⁺ to form clusters when
450 substituting for Si⁴⁺ in cristobalite (Liu et al. 2016). The impurity-poor VPC rims are mostly
451 homogeneous at the atomic scale, except for in the one case where a ~7-10 nm wide Al³⁺-
452 rich linear feature was observed (Fig. 4d,f). The significance of this feature is not explicitly
453 known, however it is similar to features previously observed in APT data from various
454 minerals (Piazolo et al. 2016, Kirkland et al. 2018, Fougrouse et al. 2019) and engineered
455 materials (Blavette et al. 1999, Miller 2006) that have been interpreted as Cottrell
456 atmospheres of trace elements decorating dislocations within crystal lattices.

457

458 **The link between impurities and crystal structure**

459 The various individual techniques used to investigate VPC crystal structure all
460 indicate an inverse relationship between $[\text{AlO}_4/\text{M}^+]^0$ concentration and degree of
461 crystallinity.

462 Weak EBSD diffraction patterns in impurity-rich crystal cores and robust patterns in
463 impurity-poor crystal rims suggest a direct link between impurity concentrations and degree
464 of long-range order in crystal frameworks (Fig. 3a). Comparison of $[\text{AlO}_4/\text{Na}^+]^0$
465 distributions (Fig. 2) and EBSD maps (Fig. 3a-c) suggest that ~2.5 wt% Al_2O_3 marks a
466 critical threshold, below which EBSD analysis confirms VPC to be highly crystalline α -
467 cristobalite, and above which VPC appears to be poorly crystalline or amorphous.

468 The CL intensity from cristobalite is known to decline during extended electron
469 radiation (Kayama et al. 2009). However, CL and EPMA mapping were concurrent in this
470 work, and performed with very short irradiation times. The observed core-to-rim variations
471 in CL intensity are therefore not considered to be a result of beam damage. Our CL results
472 contradict some previous interpretations of cristobalite luminescence. Kayama et al. (2009)
473 observed core-to-rim increases in CL intensity within natural VPC crystals from rhyolitic
474 and andesitic lavas, identical to the patterns seen in VPC from Cordón Caulle (Fig. 3d).
475 However, they attributed the luminescence to $[\text{AlO}_4/\text{Na}^+]^0$ impurities, which would suggest
476 that impurity-rich cores should show stronger luminescence than the impurity-poor rims.
477 Our analysis suggests that this is not the case, and we note that the correlation between
478 Al_2O_3 concentration and CL intensity shown by Kayama et al. (2009) is not only weak, it
479 does not take into account spatial heterogeneity of Al_2O_3 within VPC crystals, and does not
480 include chemical analysis of their non-luminescent VPC cores. We note that poor
481 luminescence can indicate that CL-active defects are sufficiently concentrated that radiative
482 transitions are suppressed ("concentration quenching"; Götze 2012), or can be a

483 consequence of the impurity-rich VPC cores being poorly crystalline or amorphous
484 (Kayama et al. 2009).

485 Laser Raman analysis is useful for discriminating between SiO₂ polymorphs (e.g.,
486 Horwell et al. 2013). The featureless spectra from impurity-rich crystal cores (Fig. 3e) could
487 mean they contain Raman-inactive β -cristobalite, or that they are poorly
488 crystalline/amorphous, lacking the diagnostic α -cristobalite peaks at ~ 230 and ~ 417 cm⁻¹
489 (Kingma and Hemley 1994), or even the ~ 400 cm⁻¹ peak sometimes seen in pure amorphous
490 SiO₂ (Bates 1972, Swainson et al. 2003).

491 Bright field and high resolution TEM images also suggest significant differences in
492 the degrees of crystallinity within VPC cores and rims. The impurity-rich cores lack long-
493 range order, appearing amorphous in high resolution images (Figs. 5c, 6), but have FFT that
494 indicate some degree of short-range order (inset to Fig. 5c) (Eckert et al. 2015). The
495 impurity-poor VPC rims have a well-developed crystal lattice that is visible in high
496 resolution images and their FFT (Fig. 5d).

497 While some of the individual techniques for investigating cristobalite crystal
498 structure can be interpreted in different ways, they all point to an inverse relationship
499 between [AlO₄/M⁺]⁰ concentration and crystal structure. Impurity-rich cores have some
500 limited short range order, whereas the impurity-poor rims are highly crystalline, tetragonal
501 α -cristobalite.

502

503 **Impurity-modulated epitaxial deposition of cristobalite**

504 The incorporation of [AlO₄/M⁺]⁰ impurities is known to have significant effects on
505 cristobalite structure and properties. Depending on their concentrations, these impurities can
506 stabilize β -cristobalite to room temperature (Chao and Lu 2002), can result in α -cristobalite
507 with a unit cell that is expanded relative to that seen in pure SiO₂ (Chao and Lu 2002).

508 Previous work on the relationship between $[\text{AlO}_4/\text{M}^+]^0$ concentrations (expressed as
509 Al_2O_3 wt%) and the size of cristobalite unit cells (as $d(111)_\beta$ and $d(101)_\alpha$) provide a
510 framework for explaining our data on Cordón Cauille VPC (Fig. 7). Theoretical d-spacings
511 for pure SiO_2 are calculated from unit cell dimensions given by Deer et al. (1992), and fall
512 within the ranges that Damby et al. (2014) compiled from PDF-2 database cards from the
513 International Centre for Diffraction Data (c.f., Fig. 1 of Damby et al. 2014). The mild
514 expansion of $d(111)_\beta$ with increasing Al_2O_3 is derived from data given by (Chao and Lu
515 2002). They reported X-ray diffraction data for synthetically Al/Na-doped β - and α -
516 cristobalite. Even at zero Al_2O_3 the d-spacings they reported were vastly different to
517 theoretical cristobalite lattice dimensions. To facilitate comparison with other data, we have
518 fit a linear function to their data on β -cristobalite, but forced it to intersect with the
519 theoretical $d(111)_\beta$ at zero Al_2O_3 (Deer et al. 1992). The more dramatic expansion of $d(101)_\alpha$
520 with increasing Al_2O_3 is derived from data given by Natrass et al. (2017). They reported 20
521 diffraction peak positions for synthetic Al/Na-doped α -cristobalite with up to 2.5 wt%
522 Al_2O_3 . The $d(101)_\alpha$ calculated from their data can be fit extremely well to a quadratic
523 function ($R^2 > 0.99$) over the range of 0 – 2.5 wt% Al_2O_3 .

524 As previously noted, Cordón Cauille VPC appears to be poorly crystalline/amorphous
525 wherever Al_2O_3 exceeds ~2.5 wt% (Figs. 2-3). Interestingly, extrapolation from the data of
526 Natrass et al. (2017) indicates that impurity concentrations ≥ 2.5 wt% Al_2O_3 will result in α -
527 cristobalite with a unit cell that is larger than the normal range of $d(101)_\alpha$ (Fig. 7). The cores
528 of natural VPC have higher impurity concentrations than investigated by Natrass et al.
529 (2017); however, EPMA and TEM data from the cores- and rims- of VPC (Figs. 5-6) plot
530 within $\pm 1\%$ of the quadratic curve to their data, even outside of their measurement ranges
531 (Fig. 7). Although this is a limited data set, it suggests that the quadratic fit to the data of
532 Natrass et al. (2017) can be reliably extrapolated to higher impurity concentrations. Doing

533 so suggests that the $d(101)_\alpha$ of highly impure α -cristobalite should converge with the $d(111)_\beta$
534 of β -cristobalite when Al_2O_3 approaches ~ 4 wt%, which approximates the maximum VPC
535 impurity concentrations measured in this study (4.17 wt. %; Table 1).

536 The ‘fish scale’ cracking observed in BSE images (Figs. 1-2; Horwell et al. 2013)
537 and grain orientations captured in EBSD (Fig. 3c; Christie et al. 1971) indicate that VPC
538 was originally deposited as β -cristobalite and subsequently underwent a transition to α -
539 cristobalite upon cooling. Following from this, declining impurity concentrations allowed
540 epitaxial lattice matching to proceed during VPC deposition and the subsequent transition
541 (Fig. 7). A steady temporal decline in $[\text{AlO}_4/\text{Na}^+]^0$ impurities within vapor-deposited layers
542 of SiO_2 would ensure that at no point during deposition were lattice mismatches between
543 subsequent layers sufficiently large to preclude deposition of the following layer. At high
544 temperatures, unit cell dimensions of β -cristobalite should have followed the gently sloping
545 curve defined by data from Chao and Lu (2002), with changes in $[\text{AlO}_4/\text{Na}^+]^0$ creating
546 negligible lattice strain. Following the $\beta \rightarrow \alpha$ transition, only the regions with < 2.5 wt%
547 Al_2O_3 are analytically identifiable as α -cristobalite; however, even in regions with higher
548 impurity concentrations, there is a regular continuum of distorted/expanded SiO_2 that grades
549 into a poorly-crystalline or partially-amorphous proxy for β -cristobalite. This is consistent
550 with the observations of Damby et al. (2014), who found natural VPC to have cell volumes
551 between those of pure α - and β -cristobalite. None of the VPC we examined appeared to
552 contain remnants of stabilized β -cristobalite, but this is likely because $[\text{AlO}_4/\text{Na}^+]^0$
553 concentrations in the natural VPC from Cordón Caulle were nowhere sufficient to fully
554 stabilize β -cristobalite to room temperature (Perrotta et al. 1989, Saltzberg et al. 1992, Chao
555 and Lu 2002, Damby et al. 2014).

556

557 **Corroded substrates for initiation of vapor deposition**

558 All observed VPC at Cordón Caulle is deposited on plagioclase (Fig. 1d-e), which is
559 enigmatic from the perspective of epitaxy. Although coordination of silica tetrahedra can
560 permit thin-film cristobalite to grow on some highly-dissimilar substrates (Jewhurst et al.
561 2005), it is difficult to reconcile how cubic (or tetragonal) cristobalite could epitaxially bind
562 to triclinic plagioclase without prohibitive angular and dimensional lattice misfits, despite
563 the chemical similarity of these phases. Incorporation of $[\text{AlO}_4/\text{M}^+]^0$ impurities themselves
564 do modify the unit cell dimensions of cristobalite (Fig. 7), but have minimal effect on high-
565 temperature β -cristobalite (Chao and Lu 2002). Furthermore, direct high resolution TEM
566 observations of plagioclase-SiO₂ boundaries in Cordón Caulle VPC do not show any
567 evidence for epitaxy across the atomically-sharp interfaces (Fig. 6).

568 The plagioclase-SiO₂ interfaces are identical to those attributed to “dissolution-
569 reprecipitation” of silicate minerals, when acids stoichiometrically dissolve mineral surfaces
570 and precipitate cation-depleted, amorphous SiO₂ layers over them (Hellmann et al. 2003,
571 Lee et al. 2007, Hellmann et al. 2012). Unlike plagioclase itself, reprecipitated amorphous
572 SiO₂ is an ideal substrate for sublimation of impurity-rich β -cristobalite, being structurally
573 similar, except with a “static” instead of “dynamic” structure (Keen and Dove 1999). The
574 interfaces observed by TEM furthermore have a sharp interface between lower- and higher-
575 density regions in poorly crystalline SiO₂ (Fig. 6, and possibly also Fig. 5c). We speculate
576 that this could be the actual interface between (1) reprecipitated plagioclase-derived
577 amorphous SiO₂; and (2) β -cristobalite (now preserved as impure and expanded α -
578 cristobalite) deposited from Si-saturated vapor.

579 Previous descriptions of VPC formation have identified glass dissolution as the
580 source of SiO₂ (Damby 2012, Schipper et al. 2015, Schipper et al. 2017), but have
581 neglected how minerals – which are more resistant to corrosion, but not inert – are also
582 affected by acidic vapor (Hellmann et al. 2003). Acidic vapor in a cooling lava body appears

583 to play two complementary roles: corroding glass to provide a source of (impure) SiO₂ that
584 is taken up into the vapor phase, while simultaneously modifying corrosion-resistant mineral
585 surfaces to provide appropriate substrates for SiO₂ deposition from that same vapor.
586 Formation of VPC is thus a natural proxy for impurity-modulated chemical vapor
587 deposition, through a process that intrinsically provides its own impurity-modulated thin-
588 film material whilst preparing its own appropriate substrate.

589

590 **Trace element transport in volcanic gases and the inferred temperatures of VPC** 591 **formation**

592 The previous sections describe how dissolution-reprecipitation of mineral surfaces
593 can prepare the plagioclase substrate for vapor deposition of VPC, and how epitaxial lattice
594 matching can occur between successive microlayers of SiO₂ with progressively declining
595 [AlO₄/Na⁺]⁰ concentrations (Fig. 7); but do not explain why [AlO₄/Na⁺]⁰ impurities
596 temporally decline during VPC deposition. Stoichiometric dissolution of volcanic glass with
597 substantial Al₂O₃ concentrations could in theory provide ample Al³⁺ throughout the VPC
598 deposition process, but this is not the case. We hypothesize that the temporal decline in
599 [AlO₄/Na⁺]⁰ impurities reflects the relative stability of metal-bearing gas species in volcanic
600 systems.

601 Measurements and/or calculations on Al- and Si-bearing volcanic gas species are few
602 in the literature, and those from rhyolitic systems are non-existent. The general stability of
603 various gas species from the well-studied Kudryavy volcano (Russia), however, can be used
604 as a proxy for investigating the stability of different species in high-temperature gases
605 (Wahrenberger 1997, Churakov et al. 2000, Henley and Seward 2018) (Fig. 8). Churakov et
606 al. (2000) identified four main Si-bearing and seven main Al-bearing species in high-T
607 gases, leading Horwell et al. (2013) to suggest SiF₄ and/or SiCl₄ to be the main gases

608 responsible for Si redistribution as VPC. The catalog of Si- and Al-bearing halogenated
609 and/or hydroxylated gas species in high-T Kudryavy gases has subsequently been expanded
610 a thermodynamic data has become available, permitting evaluation of gas-solid reactions
611 with additional species (H_4SiO_4 , $\text{Al}(\text{OH})_3$, and $\text{AlF}(\text{OH})_2$) that were not previously
612 considered (Henley and Seward 2018) (Fig. 8).

613 The first item of note is that within the suite of halogen gases, fluorinated Si and Al
614 complexes are vastly more stable than chlorinated ones in high temperature volcanic gases
615 (Fig. 8), which further supports the idea that HF is a necessary corroding agent and
616 transportation precursor gas for VPC formation. During cooling of equilibrium volcanic gas
617 from the Cordón Caulle eruption temperature (870 – 910 °C, Castro et al. 2013), all the
618 investigated Al-bearing species quickly become unstable in the gas phase (Fig. 8). Most of
619 the Si-bearing halides also become unstable, but the persistence of H_4SiO_4 across a large
620 temperature interval indicates that an Al-depleted bulk gas phase will still contain significant
621 amounts of Si that is available for deposition of VPC. A rapid decline in all Al-bearing gas
622 species during the isobaric cooling of volcanic gases in pores of the Cordón Caulle lava flow
623 is therefore inferred to have increasingly limited Al availability in the vapor from which
624 VPC was deposited, resulting in the observed core-to-rim decline in $[\text{AlO}_4/\text{Na}^+]^0$ impurities.
625 Thus, the observed impurity distributions in Cordón Caulle VPC highlight the crudeness of
626 bulk approaches that neglect the thermodynamics of gas-solid reactions in volcanic systems.

627 The actual temperature interval over which VPC forms is poorly constrained, but can
628 be bracketed by various pieces of circumstantial evidence. The maximum temperature
629 should be that of the magma storage conditions immediately before eruption, petrologically
630 defined as 870-910 °C by Castro et al. (2013). The absolute minimum temperature will be
631 that of the $\beta \rightarrow \alpha$ transition, which is nominally ~240 °C (Horwell et al. 2013), but is
632 somewhat lower and over a broader interval in impure volcanic cristobalite (Damby et al.

633 2014). Field studies have shown that when ~1 m long silica tubes are placed in high-
634 temperature fumaroles to generate a temperature gradient of ~900 – 500 °C along their full
635 lengths, cristobalite is the first mineral to form at the hot end of the tubes (Le Guern and
636 Bernard 1982, Symonds et al. 1987). This suggests that the minimum temperature of
637 cristobalite deposition is much higher. The rapid deposition of cristobalite from high-
638 temperature fumarolic gases has been attributed to the relatively low “volatility” (tendency
639 to exist in the gas phase) of Si and the cations substituted into SiO₂ (Symonds et al. 1987)
640 (e.g., Fig. 8). For comparison, several methods of industrial Chemical Vapor Deposition of
641 SiO₂ thin films are often performed at ~400-450 °C (Foggiato 2001).

642

643

Implications

644 Implications for volcanic hazards

645 The potential importance of cristobalite was brought to the attention of the
646 volcanological community when its presence was noticed in ash from Soufrière Hills
647 Volcano, Montserrat (Baxter et al. 1999). Because cristobalite is toxic if inhaled, the concern
648 was that people living near active volcanoes would be at high risk for developing chronic
649 respiratory diseases (Horwell et al. 2012). Studies that have directly addressed the toxicity
650 of volcanic cristobalite have found it to be less bio-reactive than some crystalline silica
651 dusts, and this has partly been attributed to impurities within volcanic cristobalite (Horwell
652 et al. 2003, Damby 2012, Damby et al. 2016, Horwell et al. 2012, Natrass et al. 2017).
653 Natrass et al. (2017) directly addressed the relationship between [AlO₄/Na⁺]⁰ impurities and
654 toxicity by preparing co-doped synthetic cristobalite and examining their reactivity in *in*
655 *vitro* assays, finding that impurities reduce cristobalite’s toxicity.

656 Our new results on the distribution of [AlO₄/Na⁺]⁰ within VPC crystals adds an
657 interesting note to the discussion of volcanic hazards. Stemming from the findings of

658 Natrass et al. (2017), it appears that the SiO₂ concentration maps of VPC (Fig. 2a) can be
659 considered analogous to maps of toxicity within individual crystals. Without detracting from
660 the important issue of ascertaining that volcanic eruptions will not cause chronic lung
661 diseases, we note that were an explosive event to fragment and mobilize the observed VPC
662 into respirable plumes, it appears that only the fragments of crystal rims would be pure SiO₂,
663 and perhaps only these would be toxic.

664

665 **Implications for igneous petrology**

666 It is worthwhile for igneous petrologists and volcanologists to look for VPC in lava
667 flows and domes, because VPC formation requires corrosion of glass by halogen gases
668 (Schipper et al. 2017). Its presence can therefore be taken as indicative that a given magma
669 body significantly degassed these potentially hazardous complexes during eruption (e.g.,
670 HF). Traditionally, however, vapor-phase cristobalite has often gone unrecognized. For
671 example, although Mt Ruapehu (New Zealand) lavas have been studied petrographically for
672 many decades (Gregg et al. 1960, Cole 1978), the VPC that abounds within them (e.g. Fig.
673 1e) has only recently been noticed (Conway 2016). Despite being chronically underreported,
674 VPC has been recognized in a vast array of volcanic rocks, that differ in chemistry and
675 setting. These range from basaltic lava flows of the Deccan Traps (Van Valkenburg and
676 Buie 1945), to volcanic domes and dome-derived ash of many intermediate compositions
677 (Baxter et al. 1999, Damby 2012, Boudon et al. 2015, Damby et al. 2016, Ivanova et al.
678 2018), to dacitic Vulcanian bombs (Schipper et al. 2017), to rhyolite lavas on land (Schipper
679 et al. 2015) and in the deep sea (Ikegami et al. 2018, Manga et al. 2018). Furthermore,
680 cristobalite (although not thought to be deposited from a vapor) is among the most common
681 forms of silica in lunar and martian rocks (Miyahara et al. 2013, Kayama et al. 2018). We
682 therefore suggest that cristobalite, while far from being the most abundant or nominally

683 stable SiO₂ polymorph on Earth, may in fact be the most *widely occurring* SiO₂ polymorph
684 in extrusive igneous rocks, and a useful indicator of gas-solid reactions in volcanic systems.

685

686 **Acknowledgements**

687 CIS acknowledges a Faculty Strategic Research Grant from Victoria University of
688 Wellington.

689

690

691

692 **References**

693

694 Aiuppa, A., Baker, D. R. and Webster, J. D. (2009) Halogens in volcanic systems. *Chem Geol*, 263, 1-18. doi:10.1016/j.chemgeo.2008.10.005

695 Balcone-Boissard, H., Villemant, B. and Boudon, G. (2010) Behaviour of halogens during
696 the degassing of felsic magmas. *Geochem Geophys Geosys*, 11, Q09005.
697 doi:10.1029/2010GC003028

698 Bates, J. B. (1972) Raman spectra of α and β cristobalite. *J Chem Phys*, 57, 4042-4047.
699 doi:10.1063/1.1678878

700 Baxter, P. J., Bonadonna, C., Dupree, R., Hards, V. L., Kohn, S. C., Murphy, M. D.,
701 Nichols, A., Nicholson, R. A., Norton, G. E., Searl, A., Sparks, R. S. J. and Vickers, B. P.
702 (1999) Cristobalite in volcanic ash of the Soufriere Hills Volcano, Montserrat, British West
703 Indies. *Science*, 283, 1142-1145.

704 Blavette, D., Cadel, E., Cojocaru-Mirédin, O. and Deconihout, B. (2010) The investigation
705 of boron-doped silicon using atom probe tomography. *IOP Conference Series: Materials
706 Science and Engineering*, 7, 012004. doi:10.1088/1757-899X/7/1/012004

707 Blavette, D., Cadel, E., Fraczkiewicz, A. and Menard, A. (1999) Three-dimensional atomic-
708 scale imaging of impurity segregation to line defects. *Science*, 286, 2317-2319.
709 doi:10.1126/science.286.5448.2317

710 Boudon, G., Balcone-Boissard, H., Villemant, B. and Morgan, D. J. (2015) What factors
711 control superficial lava dome explosivity? *Sci Reps*, 5, 14551. doi:10.1038/srep14551

712 Buerger, M. J. (1954) The stuffed derivatives of the silica structures. *Amer Mineral*, 39,
713 600-614.

714 Castro, J. M., Schipper, C. I., Amigo, A., Silva Parejas, C., Mueller, S., Jacob, D. and
715 Militzer, A. S. (2013) Storage and eruption of near-liquidus rhyolite magma at Cordón
716 Caulle, Chile. *Bull Volcanol*, 75, 702. doi:10.1007/s00445-013-0702-9

717 Chao, C.-H. and Lu, H.-Y. (2002) Stress-induced $\beta \rightarrow \alpha$ -cristobalite phase transformation in
718 (Na₂O+Al₂O₃)-codoped silica. *Mat Sci Eng A*, 328, 267-276.

- 719 Chao, C.-H. and Lu, H.-Y. (2002) β -cristobalite stabilization in (Na₂O + Al₂O₃)- added
720 silica. *Metal and Mater Trans A*, 33A, 2703-2711.
- 721 Christie, J. M., Lally, J. S., Heuer, A. H., Fisher, R. M., Griggs, D. T. and Radcliffe, S. V.
722 (1971) Comparative electron petrography of Apollo 11, Apollo 12, and terrestrial rocks.
723 *Proc Second Lunar Sci Conf*, 1, 69-89.
- 724 Churakov, S. V., Tkachenko, S. I., Korzhinskii, M. A., Bocharnikov, R. E. and
725 Schmulovich, K. I. (2000) Evolution of composition of high- temperature fumarolic gases
726 from Kudryavy Volcano, Iturup, Kuril Islands: the thermodynamic modeling. *Geochem Int*,
727 38, 436-451.
- 728 Cole, J. W. (1978) Andesites of the Tongariro Volcanic Centre, North Island, New Zealand.
729 *J Volcanol Geotherm Res*, 3, 121-153.
- 730 Damby, D. E., Llewellyn, E. W., Horwell, C. J., Williamson, B. J., Najorka, J., Cressey, G.
731 and Carepenter, M. (2014) The α - β phase transition in volcanic cristobalite. *J Appl Cryst*,
732 47, 1205-1215. doi:10.1107/S160057671401070X
- 733 Damby, D. E., Murphy, F. A., Horwell, C. J., Raftis, J. and Donaldson, K. (2016) The in
734 vitro respiratory toxicity of cristobalite-bearing volcanic ash. *Environ Res*, 145, 74-84.
735 doi:10.1016/j.envres.2015.11.020
- 736 de Hoog, J. C. M., van Bergen, M. J. and Jacobs, M. H. G. (2005) Vapor-phase
737 crystallisation of silica from SiF₄-bearing volcanic gases. *Annal Geophys*, 48, 775-785.
- 738 Downs, R. T. and Palmer, D. C. (1994) The pressure behavior of α cristobalite. *Amer*
739 *Mineral*, 79, 9-14.
- 740 Eckert, J., Gourdon, O., Jacob, D. E., Meral, C., Monteiro, P. J. M., Vogel, S. C., Wirth, R.
741 and Wenk, H.-R. (2015) Ordering of water in opals with different microstructures. *Eur J*
742 *Mineral*, 27, 203-213.
- 743 Fougereuse, D., Reddy, S. M., Kirkland, C. L., Saxey, D. W., Rickard, W. D. A. and Hough,
744 R. M. (2019) Time-resolved, defect-hosted, trace element mobility in deformed
745 Witwatersrand pyrite. *Geosci Front*, 10, 55-63. doi:10.1016/j.gsf.2018.03.010
- 746 Fougereuse, D., Reddy, S. M., Saxey, D. W., Rickard, W. D. A., van Riessen, A. and
747 Micklethwaite, S. (2016) Nanoscale gold clusters in arsenopyrite controlled by growth rate
748 not concentration: Evidence from atom probe microscopy. *Amer Mineral*, 101, 1916-1919.
749 doi:10.2138/am-2016-5781CCBYNCND
- 750 Francois-Saint-Cyr, H. G., Stevie, F. A., McKinley, J. M., Elshot, K., Chow, L. and
751 TRichardson, K. A. (2003) Diffusion of 18 elements implanted into thermally grown SiO₂. *J*
752 *Appl Phys*, 94, 7433-7439. doi:10.1063/1.1624487
- 753 Götze, J. (2012) Application of cathodoluminescence microscopy and spectroscopy in
754 geosciences. *Microsc Microanal*, 18, 1270-1284. doi:10.1017/S1431927612001122
- 755 Gualda, G. A. R. and Ghiorso, M. S. (2013) Low-pressure origin of high-silica rhyolites and
756 granites. *J Geol*, 121, 537-545. doi:10.1086/671395

- 757 Heaney, P. J. (1994) Structure and chemistry of the low-pressure silica polymorphs. *Rev*
758 *Mineral*, 29, 1-40.
- 759 Hellmann, R., Penisson, J.-M., Hervig, R. L., Thomassin, J.-H. and Abrioux, M.-F. (2003)
760 An EFTEM/HRTEM high-resolution study of the near surface of labradorite feldspar altered
761 at acid pH: evidence for interfacial dissolution-precipitation. *Phys Chem Minerals*, 30,
762 192-197. doi:10.1007/s00269-003-0308-4
- 763 Hellmann, R., Wirth, R., Daval, D., Barnes, J.-P., Penisson, J.-M., Tisserand, D., Epicier, T.,
764 Florin, B. and Hervig, R. L. (2012) Unifying natural and laboratory chemical weathering
765 with interfacial dissolution– precipitation: A study based on the nanometer-scale
766 chemistry of
767 fluid–silicate interfaces. *Chem Geol*, 294-295, 203-216. doi:10.1016/j.chemgeo.2011.12.002
- 768 Henley, R. W. and Seward, T. M. (2018) Gas-solid reactions in arc volcanoes: Ancient and
769 modern. *Rev Mineral Geochem*, 84, 309-349. doi:10.2138/rmg.2018.84.9
- 770 Horwell, C. J., Fenoglio, I., Ragnarsdottir, K. V., Sparks, R. S. J. and Fubini, B. (2003)
771 Surface reactivity of volcanic ash from the eruption of Soufrière Hills volcano, Montserrat,
772 West Indies with implications for health hazards. *Envir Res*, 93, 202-215.
773 doi:10.1016/S0013-9351(03)00044-6
- 774 Horwell, C. J., Hillman, S. E., Cole, P. D., Loughlin, S. C., Llewellyn, E. W., Damby, D. E.
775 and Christopher, T. E. (2014) Controls on variations in cristobalite abundance in ash
776 generated by the Soufrière Hills Volcano, Montserrat in the period 1997-2010. *Geol Soc*
777 *London Memoirs*, 39, 399-406. doi:10.1144/M39.21
- 778 Horwell, C. J., Williamson, B. J., Donaldson, K., Le Blond, J. S., Damby, D. E. and Bowen,
779 L. (2012) The structure of volcanic cristobalite in relation to its toxicity; relevance for the
780 variable crystalline silica hazard. *Particle and Fibre Tech*, 9, 44.
- 781 Horwell, C. J., Williamson, B. J., Llewellyn, E. W., Damby, D. E. and Le Blond, J. S. (2013)
782 The nature and formation of cristobalite at the Soufrière Hills volcano, Montserrat:
783 implications for the petrology and stability of silicic lava domes. *Bull Volcanol*, 75, 696.
784 doi:10.1007/s00445-013-0696-3
- 785 Ikegami, F., McPhie, J., Carey, R., Mundana, R., Soule, A. and Jutzeler, M. (2018) The
786 eruption of submarine rhyolite lavas and domes in the deep ocean - Havre 2012, Kermadec
787 Arc. *Front Earth Sci*, 6, 147. doi:10.3389/feart.2018.00147
- 788 Ivanova, D. A., Shcherbakov, V. D., Plechov, P. Y., Nekrylov, N. A., Davydova, V. O.,
789 Turova, M. A. and Stepanov, O. V. (2018) Cristobalite in extrusive rocks of Bezymianny
790 volcano. *New data on minerals*, 52, 51-58.
- 791 Jewhurst, S. A., Andeen, D. and Lange, F. F. (2005) Crystal chemistry of the epitaxy of
792 cristobalite (SiO₂) on basal plane sapphire. *J Cryst Growth*, 280, 168-172.
793 doi:10.1016/j.jcrysgro.2005.03.031
- 794 Kayama, M., Nagaoka, H. and Niihara, T. (2018) Lunar and Martian Silica. *Minerals*, 8,
795 267. doi:10.3390/min8070267

- 796 Kayama, M., Nishido, H. and Ninagawa, K. (2009) Cathodoluminescence characterization
797 of tridymite and cristobalite: Effects of electron irradiation and sample temperature. *Amer*
798 *Mineral*, 94, 1018-1028. doi:10.2138/am.2009.3133
- 799 Kayama, M., Nishido, H. and Ninagawa, K. (2009) Effect of impurities on
800 cathodoluminescence of tridymite and cristobalite. *J Mineral Petrol Sci*, 104, 401-406.
801 doi:10.2465/jmps.090620a
- 802 Keen, D. A. and Dove, M. T. (1999) Local structures of amorphous and crystalline phases of
803 silica, SiO₂, by neutron total scattering. *J Phys Condens Matter*, 11, 9263-9273.
- 804 Kingma, K. J. and Hemley, R. J. (1994) Raman spectroscopic study of microcrystalline
805 silica. *Am Mineral*, 79, 269-273.
- 806 Kirkland, C. L., Fougereuse, D., Reddy, S. M., Hollis, J. and Saxey, D. W. (2018) Assessing
807 the mechanisms of common Pb incorporation into titanite. *Chem Geol*, 483, 558-566.
808 doi:10.1016/j.chemgeo.2018.03.026
- 809 Klaus, J. W. and George, S. M. (2000) SiO₂ chemical vapor deposition at room temperature
810 using SiCl₄ and H₂O with an NH₃ catalyst. *J Electrochem Soc*, 147, 2658-2664.
811 doi:10.1.1.909.4760
- 812 Le Guern, F. and Bernard, A. (1982) A new method for sampling and analyzing volcanic
813 sublimates - Application to Merapi Volcano, Java. *J Volcanol Geotherm Res*, 12, 133-146.
- 814 Lee, M. R., Brown, D. J., Smith, C. L., Hodson, M. E., MacKenzie, M. and Hellmann, R.
815 (2007) Characterization of mineral surfaces using FIB and TEM: A case study of naturally
816 weathered alkali feldspars. *Amer Mineral*, 92, 1383-1394. doi:10.2138/am.2007.2453
- 817 Liu, J., Wang, Y. and An, L. (2016) Abnormal behavior of silica doped with small amounts
818 of aluminum. *Sci Reps*, 6, 35556. doi:10.1038/srep35556
- 819 Manga, M., Mitchell, S. J., Degruyter, W. and Carey, R. J. (2018) Transition of eruptive
820 style: Pumice raft to dome-forming eruption at the Havre submarine volcano, southwest
821 Pacific Ocean. *Geology*, 46, 1075-1078. doi:10.1130/G45436.1
- 822 Miller, M. K. (2006) Atom probe tomography characterization of solute segregation to
823 dislocations. *Microscopy Res Tech*, 69, 359-365. doi:10.1002/jemt.20291
- 824 Miyahara, M., Kaneko, S., Ohtani, E., Sakai, T., Nagase, T., Kayama, M., Nishido, H. and
825 Hirao, N. (2013) Discovery of seifertite in a shocked lunar meteorite. *Nature Comms*, 4,
826 1737. doi:10.1038/ncomms2733
- 827 Moore, R. E. and Karakus, M. (1994) Cathodoluminescence Microscopy, A Technique
828 Uniquely Suited to the Solution of Refractory Wear Problems. *Proc. of the International*
829 *Ceramics Conference (Austceram'94)*, 925-940.
- 830 Nakahata, K., Ro, K., Suemasu, A., Kamiya, T., Fortmann, C. M. and Smimizu, I. (2000)
831 Fabrication of polycrystalline silicon films from SiF₄/H₂/SiH₄ gas mixture using very high
832 frequency plasma enhanced chemical vapor deposition with in situ plasma diagnostics and
833 their structural properties. *Jpn J Appl Phys*, 39, 3294-3301. doi:10.1143/JJAP.39.3294

- 834 Natrass, C., Horwell, C. J., Damby, D. E., Brown, D. and Stone, V. (2017) The effect of
835 aluminium and sodium impurities on the in vitro toxicity and pro-inflammatory potential of
836 cristobalite. *Environ Res*, 159, 164-175. doi:10.1016/j.envres.2017.07.054
- 837 Oelkers, E. H. (2001) General kinetic description of multioxide silicate mineral and glass
838 dissolution. *Geochim Cosmochim Acta*, 65, 3703-3719.
- 839 Pankrath, R. and Flörke, O. W. (1994) Kinetics of Al-Si exchange in low and high quartz:
840 calculation of Al diffusion coefficients. *Eur J Mineral*, 6, 435-457.
841 doi:10.1127/ejm/6/4/0435
- 842 Perrotta, A. J., Grubbs, D. K., Martin, E. S., Dando, N. R., McKinstry, H. A. and Huang, C.-
843 Y. (1989) Chemical stabilization of β -cristobalite. *J Am Ceram Soc*, 72, 441-447.
844 doi:10.1111/j.1151-2916.1989.tb06150.x
- 845 Piazzolo, S., La Fontaine, A., Trimby, P., Harley, S., Yang, L., Armstrong, R. and Cairney, J.
846 M. (2016) Deformation-induced trace element redistribution in zircon revealed using atom
847 probe tomography. *Nature Comms*, 7, 10490. doi:10.1038/ncomms10490
- 848 Raghuvanshi, M., Lanterne, A., Le Perchec, J., Pareige, P., Cadel, E., Gall, S. and Duguay,
849 S. (2015) Influence of boron clustering on the emitter quality of implanted silicon solar
850 cells: an atom probe tomography study. *Prog Photovolt Res Appl*, 23, 1724-1733.
851 doi:10.1002/pip.2607
- 852 Reddy, S. M., van Riessen, A., Saxey, D. W., Johnson, T. E., Rickard, W. D. A.,
853 Fougereuse, D., Fischer, S., Prosa, T. J., Rice, K. P., Reinhard, D. A., Chen, Y. and Olson,
854 D. (2016) Mechanisms of deformation-induced trace element migration in zircon resolved
855 by atom probe and correlative microscopy. *Geochim Cosmochim Acta*, 195, 158-170.
856 doi:10.1016/j.gca.2016.09.019
- 857 Saltzberg, M. A., Bors, S. L., Bergna, H. and Winchester, S. C. (1992) Synthesis of
858 chemically stabilized cristobalite. *J Am Ceram Soc*, 75, 89-95.
- 859 Schipper, C. I., Castro, J. M., Kennedy, B. M., Christenson, B. W., Aiuppa, A., Alloway, B.
860 V., Forte, P., Seropian, G. and Tuffen, H. (2019) Halogen (Cl, F) and sulphur release during
861 explosive, effusive, and intrusive phases of the 2011 rhyolitic eruption at Cordón Caulle
862 volcano (Chile). *Volcanica*, 2, 73-90. doi:10.30909/vol.02.01.7390
- 863 Schipper, C. I., Castro, J. M., Tuffen, H., James, M. R. and How, P. (2013) Shallow vent
864 architecture during hybrid explosive-effusive activity at Cordón Caulle (Chile, 2011-12):
865 Evidence from direct observations and pyroclast textures. *J Volcanol Geotherm Res*, 262,
866 25-37. doi:10.1016/j.jvolgeores.2013.06.005
- 867 Schipper, C. I., Castro, J. M., Tuffen, H., Wadsworth, F. B., Chappell, D., Pantoja, A. E.,
868 Simpson, M. and Le Ru, E. C. (2015) Cristobalite in the 2011-12 Cordón Caulle eruption
869 (Chile). *Bull Volcanol*, 77, 34. doi:10.1007/s00445-015-0925-z
- 870 Schipper, C. I., Mandon, C., Maksimenko, A., Castro, J. M., Conway, C. E., Hauer, P.,
871 Kirilova, M. and Kilgour, G. (2017) Vapor-phase cristobalite as a durable indicator of
872 magmatic pore structure and halogen degassing: An example from White Island volcano
873 (New Zealand). *Bull Volcanol*, 79, 74. doi:10.1007/s00445-017-1157-1

- 874 Smith, J. V. and Steele, I. M. (1984) Chemical substitution in silica polymorph. Neues Jahrb
875 Miner Monat, 3, 137-144.
- 876 Swainson, I. P., Dove, M. T. and Palmer, D. C. (2003) Infrared and Raman spectroscopy
877 studies of the α - β transition in cristobalite. Phys Chem Minerals, 30, 353-365.
878 doi:10.1007/s00269-003-0320-8
- 879 Swanson, S. E., Naney, M. T., Westrich, H. R. and Eichelberger, J. C. (1989) Crystallization
880 history of Obsidian Dome, Inyo Domes, California. Bull Volcanol, 51, 161-176.
- 881 Symonds, R. B., Rose, W. I., Reed, M. H., Lichte, F. E. and Finnegan, D. L. (1987)
882 Volatilization, transport and sublimation of metallic and non-metallic elements in high
883 temperature gases at Merapi Volcano, Indonesia. Geochim Cosmochim Acta, 51, 2083-
884 2101.
- 885 Tuffen, H., James, M. R., Castro, J. M. and Schipper, C. I. (2013) Exceptional mobility of an
886 advancing rhyolitic obsidian flow at Cordón Caulle volcano in Chile. Nature Comm, 4,
887 2709. doi:10.1038/ncomms3709
- 888 Van Valkenburg, A. and Buie, B. F. (1945) Octahedral cristobalite with quartz paramorphs
889 from Ellora Caves, Hyderabad State, India. Amer Mineral, 30, 526-535.
- 890 Withers, R. L., Thompson, J. G. and Welberry, T. R. (1989a) The structure and
891 microstructure of α -cristobalite and its relationship to β -cristobalite. Phys Chem Minerals,
892 16, 517-523.
- 893 Withers, R. L., Welberry, T. R., Hua, G. L., Thompson, J. G. and Hyde, B. G. (1989b) A
894 transmission electron microscopy study of cristobalite. Phase Trans, 16, 41-45.
895 doi:10.1080/01411598908245678
- 896 Wolff-Boenisch, D., Gislason, S. R. and Oelkers, E. H. (2004) The effect of fluoride on the
897 dissolution rates of natural glasses at pH 4 and 25°C. Geochim Cosmochim Acta, 68, 4571-
898 4582. doi:10.1016/j.gca.2004.05.026
- 899 Wu, Y.-F., Fougereuse, D., Evans, K. A., Reddy, S. M., Saxey, D. W., Guagliardo, P. and
900 Li, J.-W. (2019) Gold, arsenic, and copper zoning in pyrite: A record of fluid chemistry and
901 growth kinetics. Geology, 47, 641-644. doi:10.1130/G46114.1

902
903

Figure Captions

904 **Figure 1.** The SiO₂ system and vapor-phase cristobalite (VPC). (a) Low-pressure phase
905 diagram for the silica system (modified from Heaney et al. 1994). Note there is no stability
906 field for α -cristobalite, which is only metastable after the $\beta \rightarrow \alpha$ transition at ~ 240 °C. The
907 pre-eruptive magma storage conditions at Cordón Caulle were at far lower temperature
908 (~ 900 °C, 50 to 100 MPa; Castro et al. 2013) than the β -cristobalite stability field. (b) SEM
909 image of a VPC crystal grown on a substrate that includes many plagioclase (+/- pyroxene)

910 microlites. The microlites are clearly visible because any glass that was originally present
911 has now been removed in the corrosion process. (c) BSE image of a VPC-bearing vesicle,
912 with a glass-free corrosion rim and many VPC crystals. (d-e) BSE images in which
913 characteristic fish scale cracking is apparent in VPC. Labels indicate vesicle (ves),
914 plagioclase (plg), pyroxene (px), and VPC. All images are from Cordón Caulle lava
915 samples, except (e), which is from an andesitic lava flow at Mt Ruapehu, shown because the
916 VPC crystal is clearly deposited on a plagioclase phenocryst.

917

918 **Figure 2.** VPC major element chemistry by EPMA. (a) BSE images of singular (Crystal
919 L10-01) and twinned (Crystal L10-07) VPC with phases marked as in Figure 1. (b-d) Maps
920 of Si, Al, and Na, plotted as wt% oxides by convention. For clarity, only data within VPC
921 crystals are shown. Ranges of each oxide are the same for both crystals. (e) Molar
922 percentages of Na^+ versus Al^{3+} , with symbols colored according to position along the core-
923 to-rim transects marked in (a). The $\text{Al}^{3+}/\text{Na}^+$ ratio of ~ 1 confirms that these impurities are of
924 the co-substitutional $[\text{AlO}_4/\text{M}^+]^0$ form. Note that L10-01 was analysed by EPMA before
925 being analysed by EBSD, and the opposite is true for L10-07. Uncertainties in EPMA
926 analysis are smaller than symbol sizes.

927

928 **Figure 3.** Structure of the same VPC crystals shown in Figure 2. (a-c) EBSD data, showing
929 band contrast (a) and diffraction pattern indexing (b) to be poor in crystal cores and strong in
930 crystal rims. (c) EBSD Euler images with orientation boundaries outlined. (d) Hyperspectral
931 CL map colored by intensity of luminescence on the ~ 2.7 eV (459 nm) band that is intrinsic
932 to cristobalite. (e) Laser Raman spectra from positions marked in (a) on Crystal L10-01
933 only, compared to characteristic α -cristobalite peak positions at 230 and 417 cm^{-1} (Kingma
934 and Hemley 1994). Some beam damage is apparent in Crystal L10-01, which was analysed

935 by EPMA before EBSD and Laser Raman, but concurrently with CL. No beam damage is
936 apparent in Crystal L10-07.

937

938 **Figure 4.** Composition of VPC by atom probe tomography. (a) VPC crystal showing liftout
939 locations of APT specimen tips (and TEM foils; Fig. 5) from the core (AP-1, TEM-1) and
940 rim (AP-2, TEM-2). Dashed white line marks EPMA spot analysis profile through this
941 crystal. (b) Example of a ranged mass-to-charge ratio spectrum for VPC. (c-d) APT
942 tomographic reconstructions showing 50% of Al atoms. Note the clustering of Al atoms in
943 (c) and the Al-rich linear feature in (d). (e) Plot of Al_2O_3 versus SiO_2 showing a good
944 agreement between bulk APT analysis (Table 2) and EPMA spot analysis. To permit
945 comparison, APT concentrations are converted from at% to equivalent wt% oxides by
946 assuming ideal oxygen:cation ratios. (f) Linear Al concentration profiles taken along the
947 cylinders shown in (c-d), highlighting the apparent sawtooth concentration profiles created
948 by Al clustering in the crystal core, and the Al-rich linear feature in the crystal rim. Average
949 analytical uncertainties are shown as ± 1 standard deviation (SD).

950

951 **Figure 5.** Structure of VPC observed by transmission electron microscopy. Foils are from
952 the core (TEM-1; a,c) and rim (TEM-2; b,d) of the VPC crystal shown in Figure 4a. (a-b)
953 Bright field TEM images with lamellae typical of the stacking faults often seen in α -
954 cristobalite (Christie et al. 1971). (c-d) High resolution images with inset FFT. Images from
955 crystal core (c) appear amorphous, but their FFT have diffuse rings at $7.07 \pm 0.08 \text{ \AA}$ that
956 suggest there to be some short-range order. Images from the crystal rim show well-defined
957 crystal lattice fringes and have FFT with bright reflections at $6.92 \pm 0.02 \text{ \AA}$.

958

959 **Figure 6.** Substrate-VPC interface. High resolution TEM image across the substrate-SiO₂
960 interface, with strong lattice fringes in the plagioclase substrate (plg), but amorphous
961 structure in the adjacent SiO₂. A region of slightly darker material (top right, marked
962 “VPC?”) has a sharp interface with the amorphous SiO₂. Inset is BSE image of VPC crystal,
963 showing location of TEM foil.

964

965 **Figure 7.** Influence of impurities on cristobalite lattice, with $d(111)_\beta$ and $d(101)_\alpha$ versus
966 $[AlO_4/M^+]^0$ dopant concentration (expressed as wt% Al₂O₃). Theoretical d-spacings
967 calculated from lattice parameters for pure SiO₂-cristobalite (Deer et al. 1992), and ICDD
968 ranges are replotted from Damby et al. (2014). Green crosses are Al/Na-doped α -cristobalite
969 from Natrass et al. (2017) with interpolated quadratic best-fit (solid green line, $R^2 > 0.99$)
970 extrapolated to ~4 wt% Al₂O₃ (dashed green line). Impurities have a comparatively minor
971 effect on $d(111)_\beta$ (Chao and Lu 2002; after their data was adjusted for comparability, see
972 text for explanation). The blue and red symbols represent data from the core (TEM-1) and
973 rim (TEM-2) of the VPC crystal shown in Figures 4-5.

974

975 **Figure 8.** Equilibrium concentrations of Si- and Al-bearing halogen and hydroxyl volcanic
976 gases, relative to inferred VPC formation and transition temperatures. Curves are calculated
977 based on high-temperature gases from Kudryavy volcano (Henley and Seward 2018,
978 Wahrenberger 1997), as a proxy for high temperature volcanic gases in general. The
979 temperature interval of SiO₂ deposition is bracketed by the Cordón Caulle eruption
980 temperature ($T_{\text{eruption}} \sim 900$ °C, Castro et al. 2013) and the $\beta \rightarrow \alpha$ transition (lower/broader
981 range for volcanic cristobalite (blue field); Damby et al. 2014, nominally ~240 °C (blue
982 dashed line; Horwell et al. 2013). The red-to-yellow faded region indicates a more likely

983 temperature range for VPC temperature based on field sampling of high-temperature
 984 fumaroles (Le Guern and Bernard 1982, Symonds et al. 1987).

985

986

987

988

Tables

Table 1. VPC composition by EPMA

wt%	Composition (wt%)			No. of spots/ No. of crystals
	Average	±1 S.D.	Min - Max	
SiO ₂	97.4	1.15	93.6 - 99.6	827 / 12
TiO ₂	0.15	0.07	b.d. - 0.37	831 / 12
Al ₂ O ₃	1.74	0.88	0.19 - 4.17	829 / 12
FeO	0.09	0.10	b.d. - 0.43	158 / 1
MgO	0.01	0.01	b.d. - 0.04	157 / 1
CaO	0.05	0.04	b.d. - 0.29	156 / 1
Na ₂ O	0.64	0.64	b.d. - 4.7	828 / 12
K ₂ O	0.05	0.06	b.d. - 0.45	830 / 12
P ₂ O ₅	0.03	0.04	b.d. - 0.15	159 / 1

989 Summary of spot analysis by EPMA. Data collected using focused beam, 15 kV accelerating
 990 voltage and either 12 or 2 nA beam current. All spot analyses are thought to have suffered
 991 some loss of Na under electron radiation. b.d. refers to below detection limit.

992

993 Table 2. VPC composition by APT

Liftout APT run number	AP-1 (Core)			AP-2 (Rim)		
	1037	1039	1344	1349	1361*	1364
Atoms (x10 ⁶)	13.6	35.4	20.0	13.7	8.8	6.3
at%						
Si	35.95	35.86	36.50	36.33	36.11	36.35
Ti	0.0039	0.0041	0.0041	0.0040	0.0034	0.0045
Al	0.836	0.985	0.257	0.303	0.330	0.339
CaO	0.0070	0.0101	0.0014	b.d.	b.d.	b.d.
Na	b.d.	b.d.	0.029	0.068	0.114	0.087
K	b.d.	b.d.	b.d.	b.d.	0.0031	b.d.
O	63.20	63.14	63.20	63.30	63.44	63.22

994 Bulk composition of the core and rim of a single VPC crystal (Fig. 4a) as determined by
 995 APT. *Tip 1361 contained the linear concentration of Al atoms illustrated in Figure 4d.

996

997

Figure 1

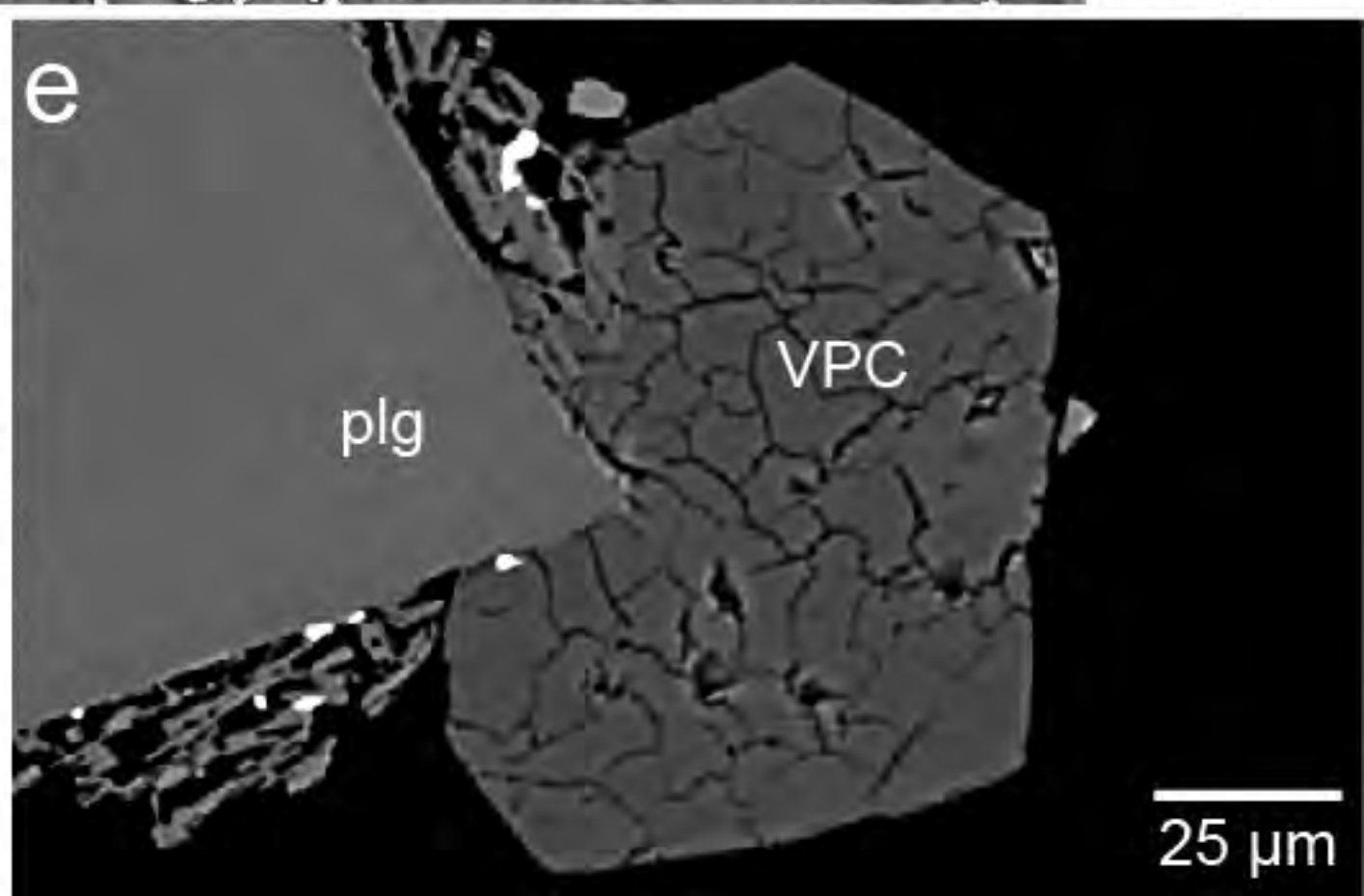
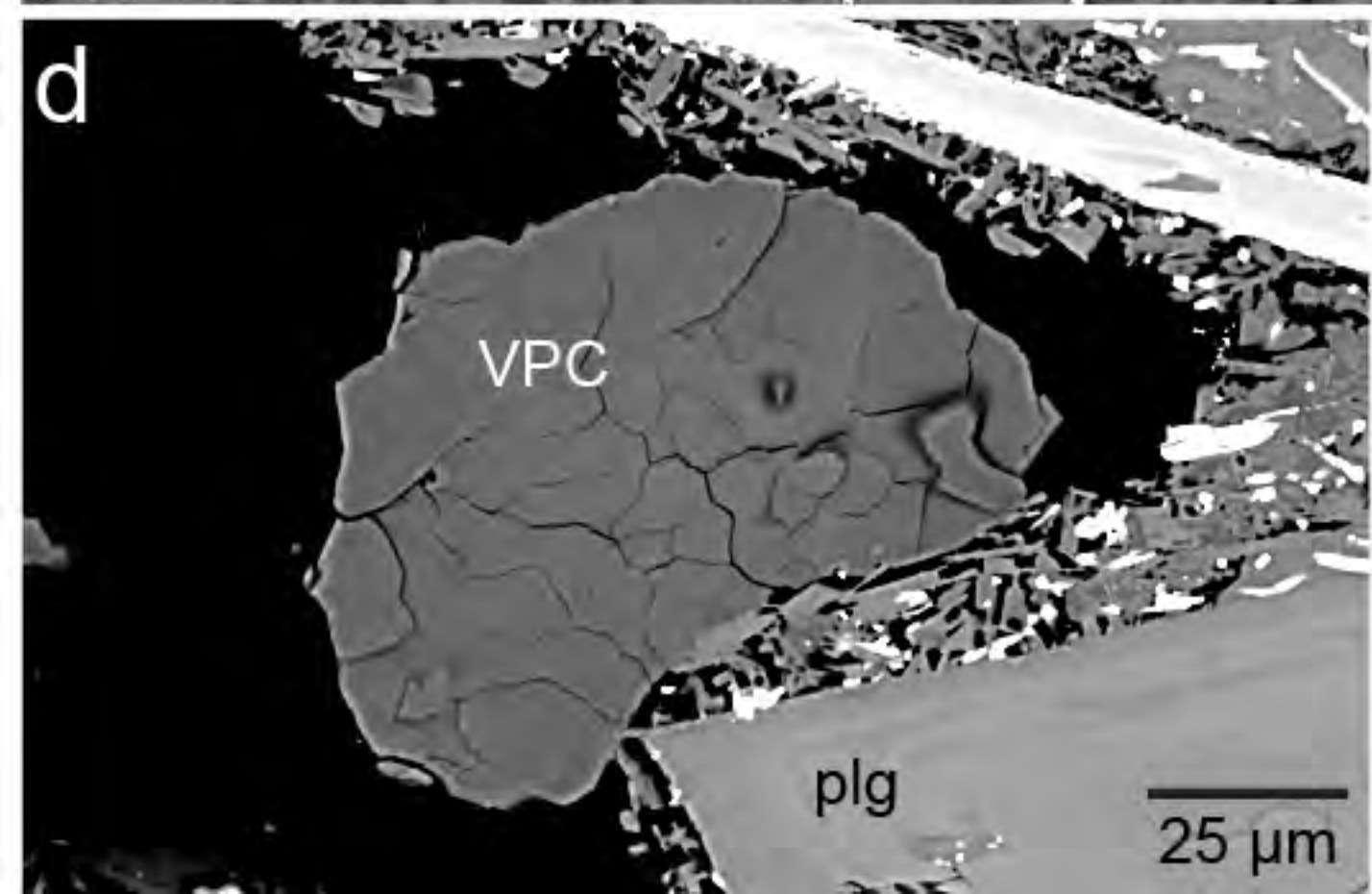
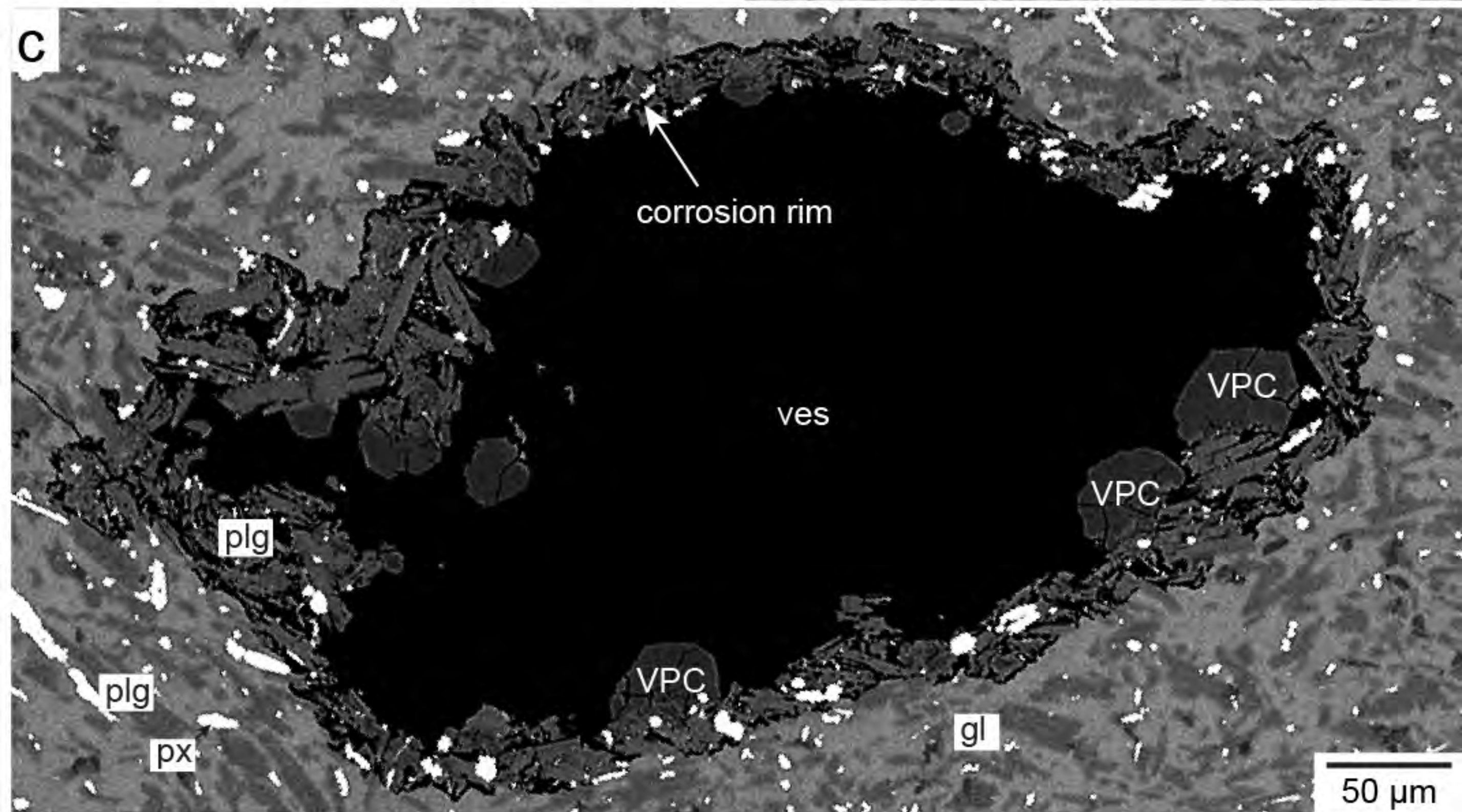
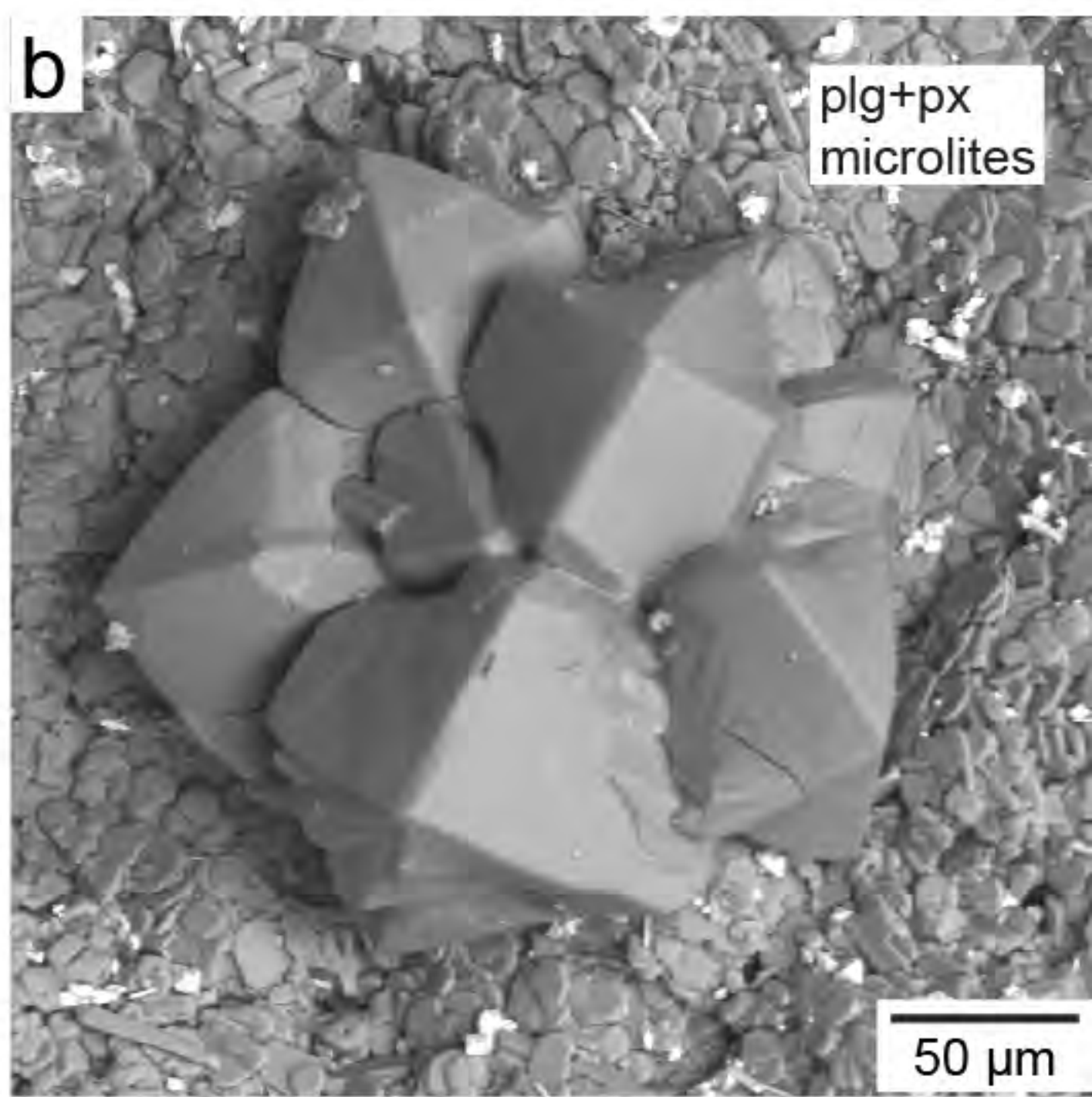
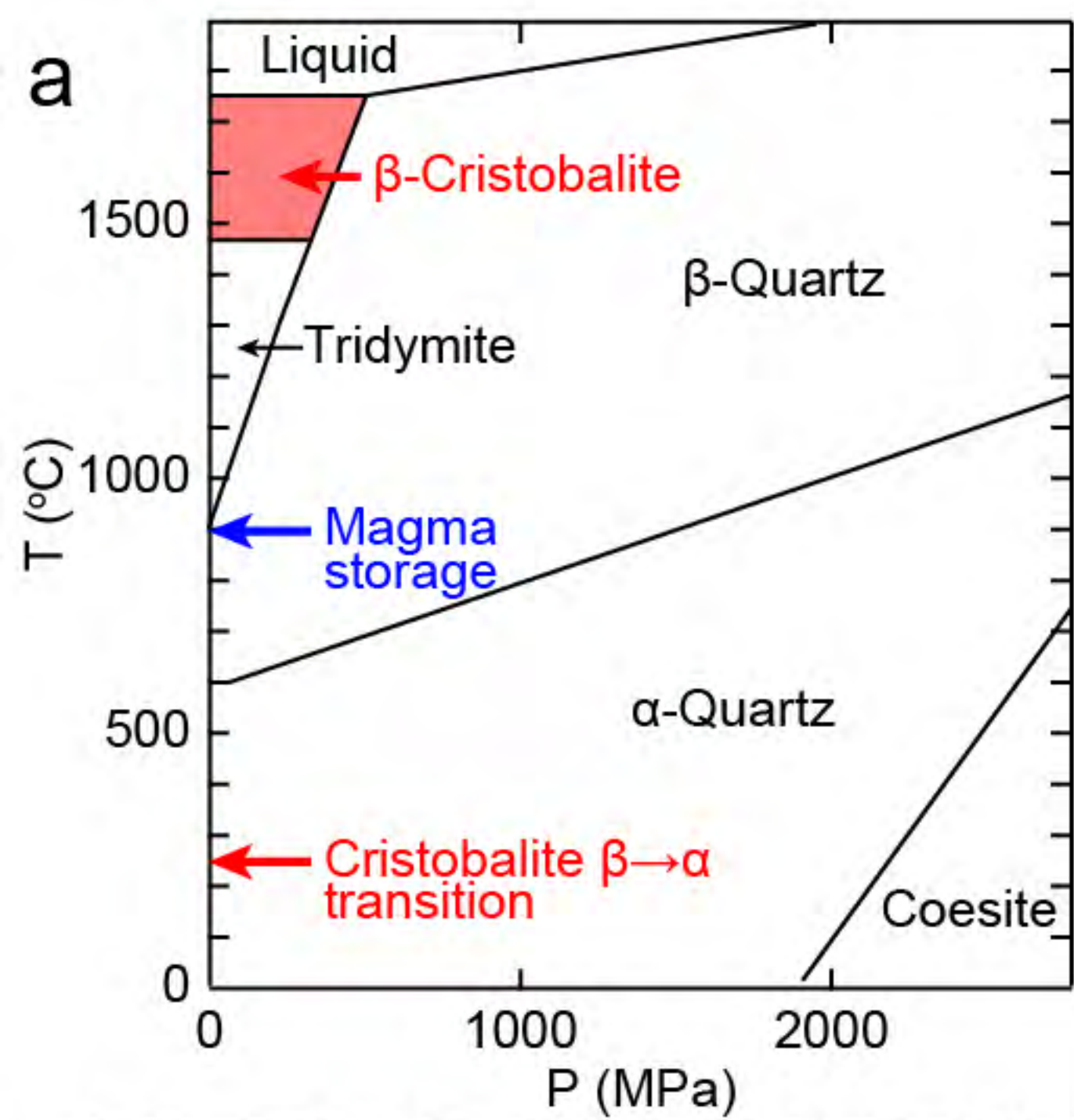


Figure 2

Crystal L10-01

Crystal L10-07

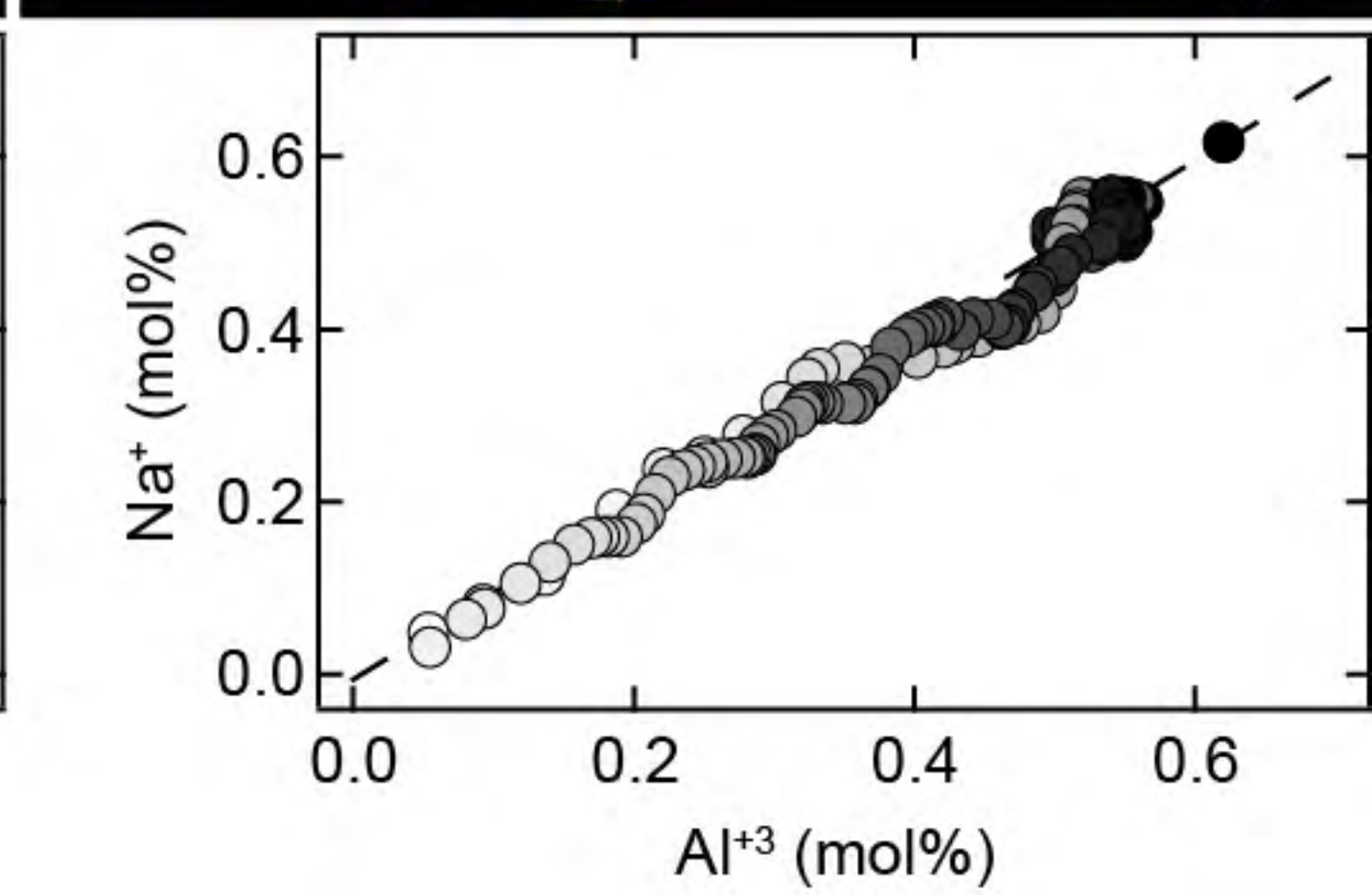
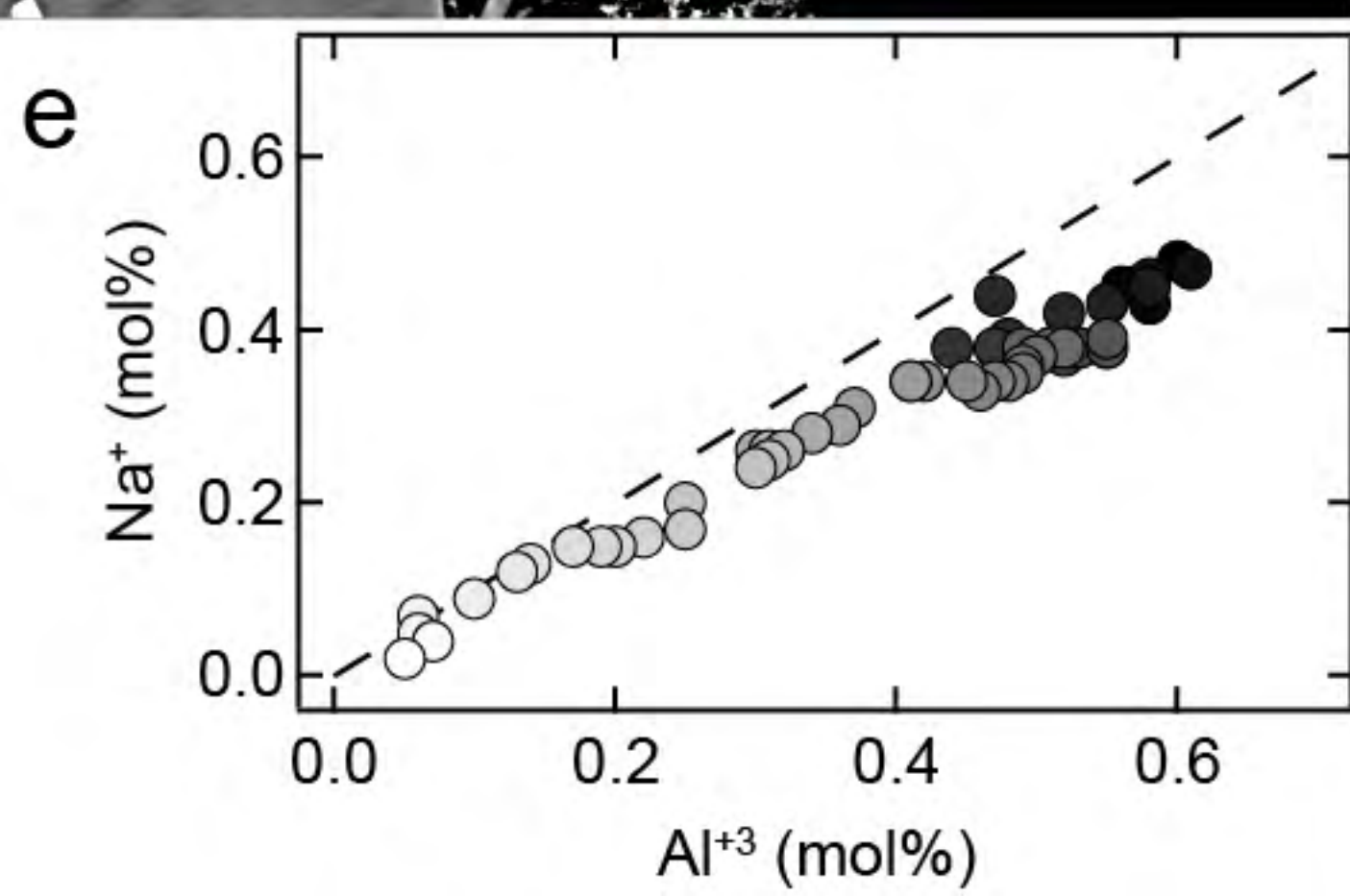
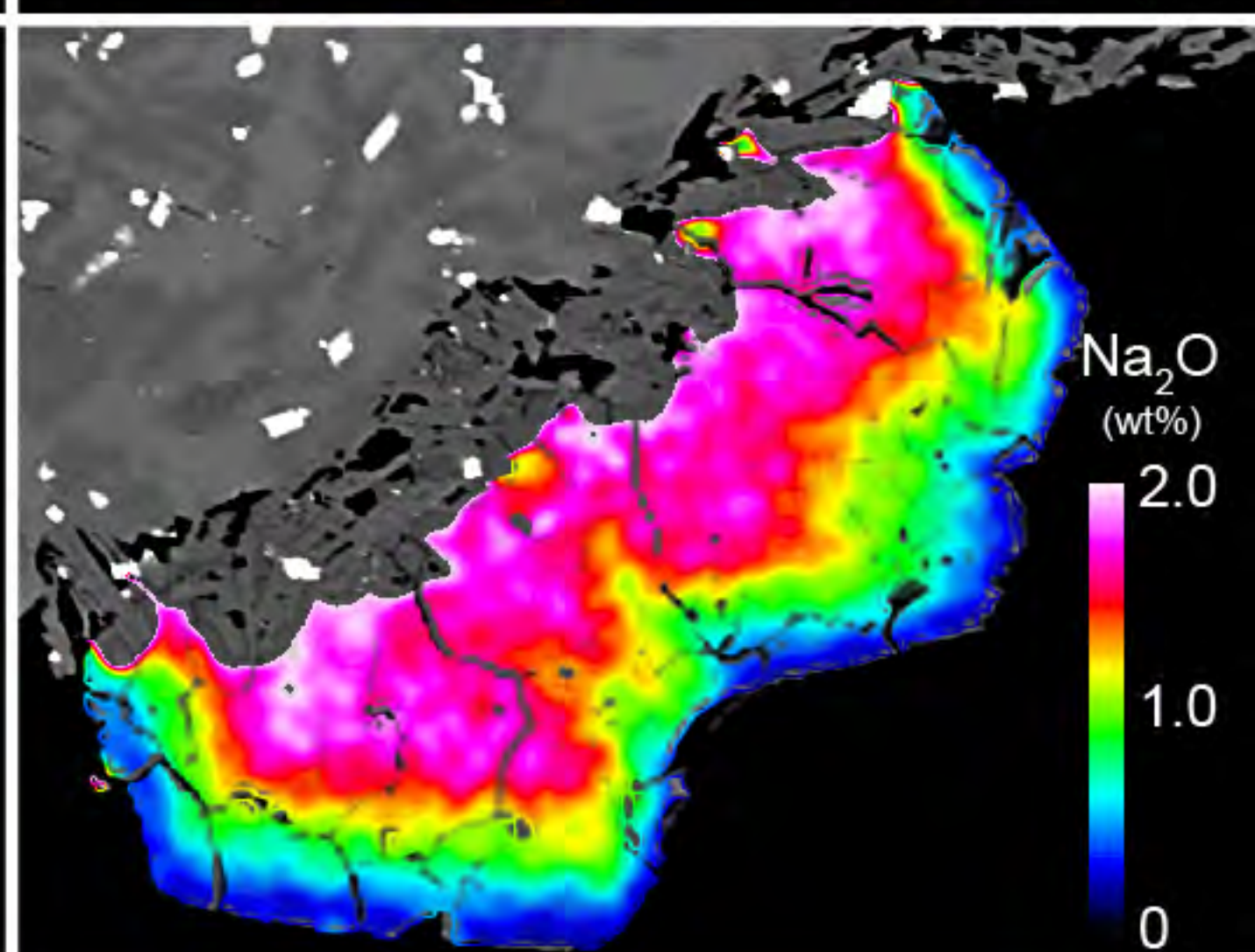
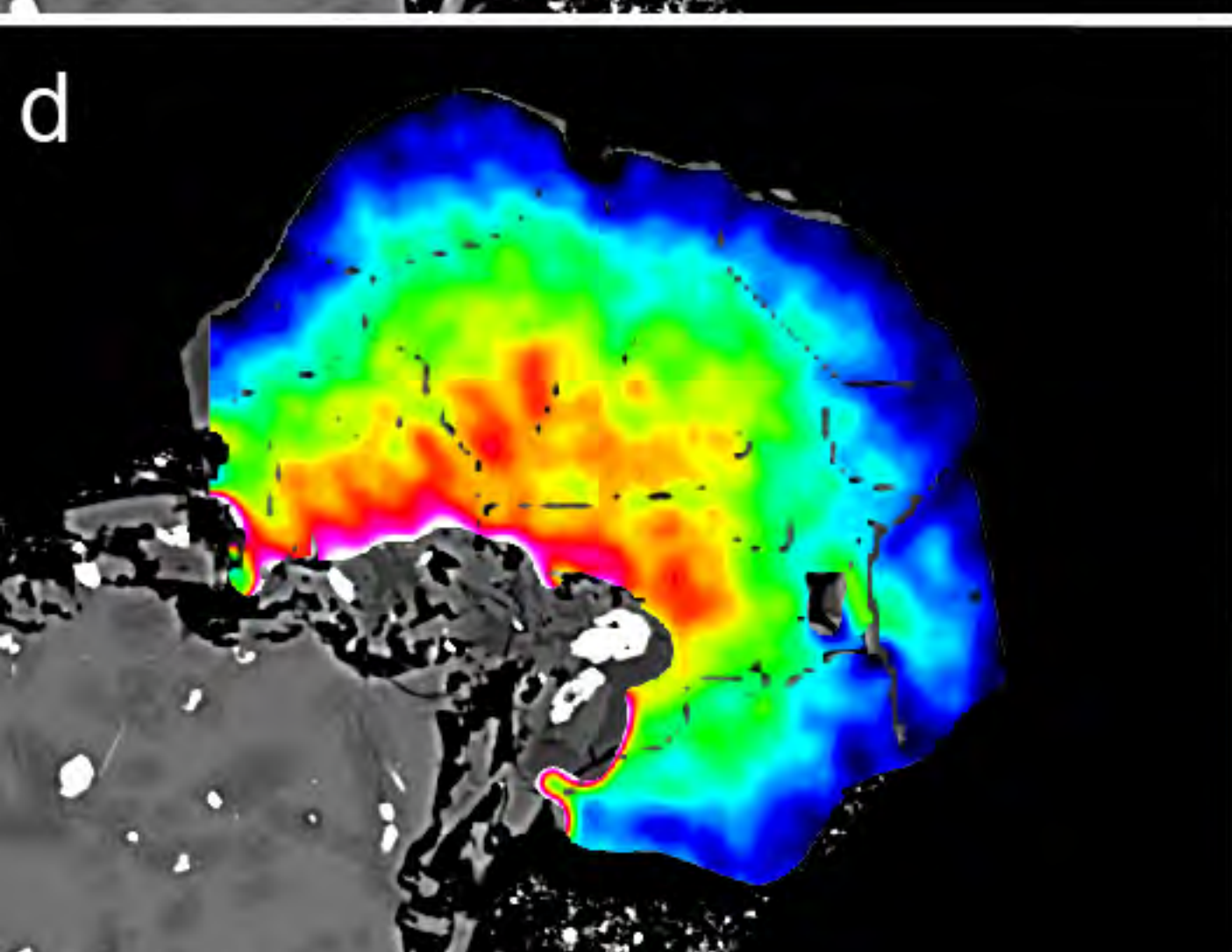
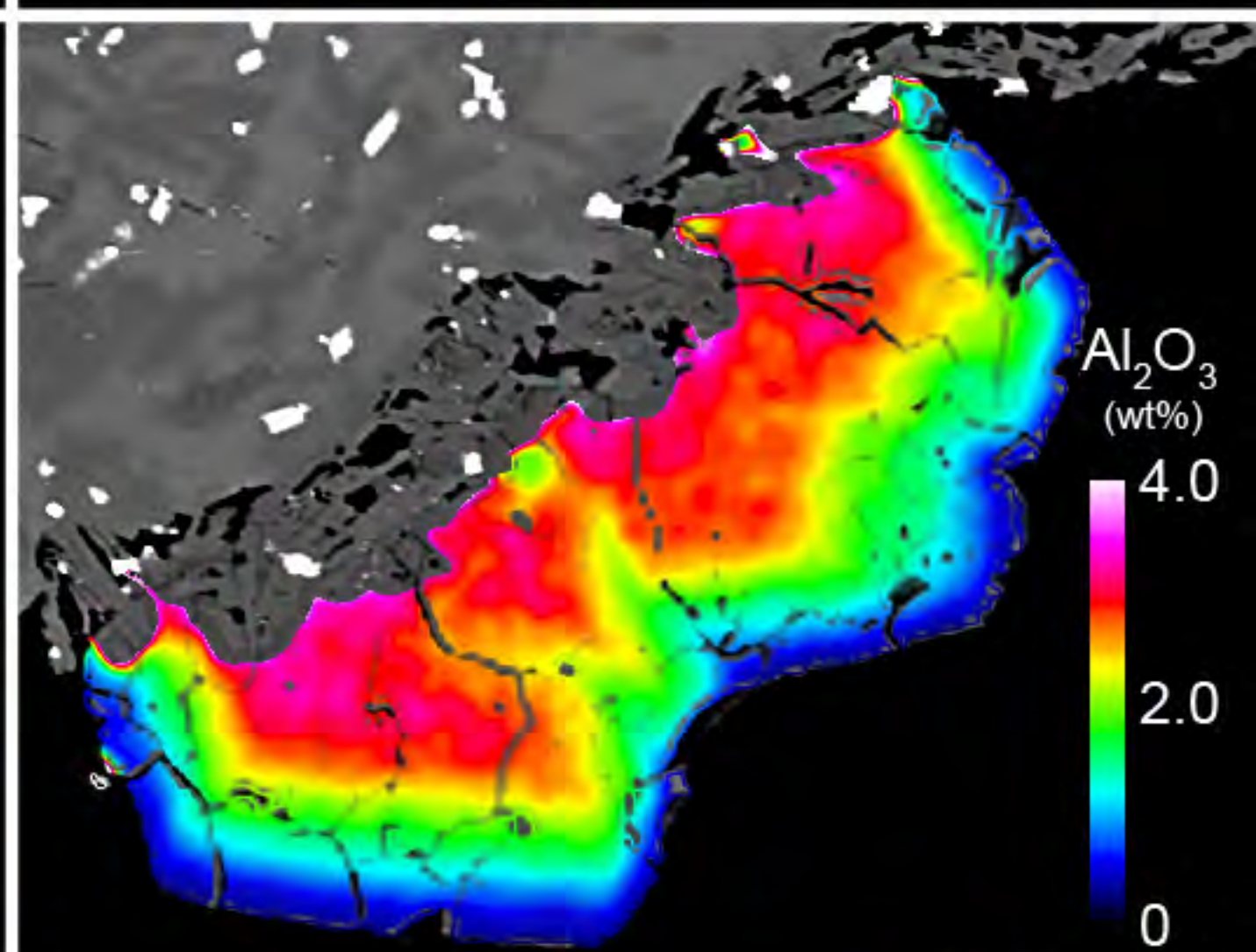
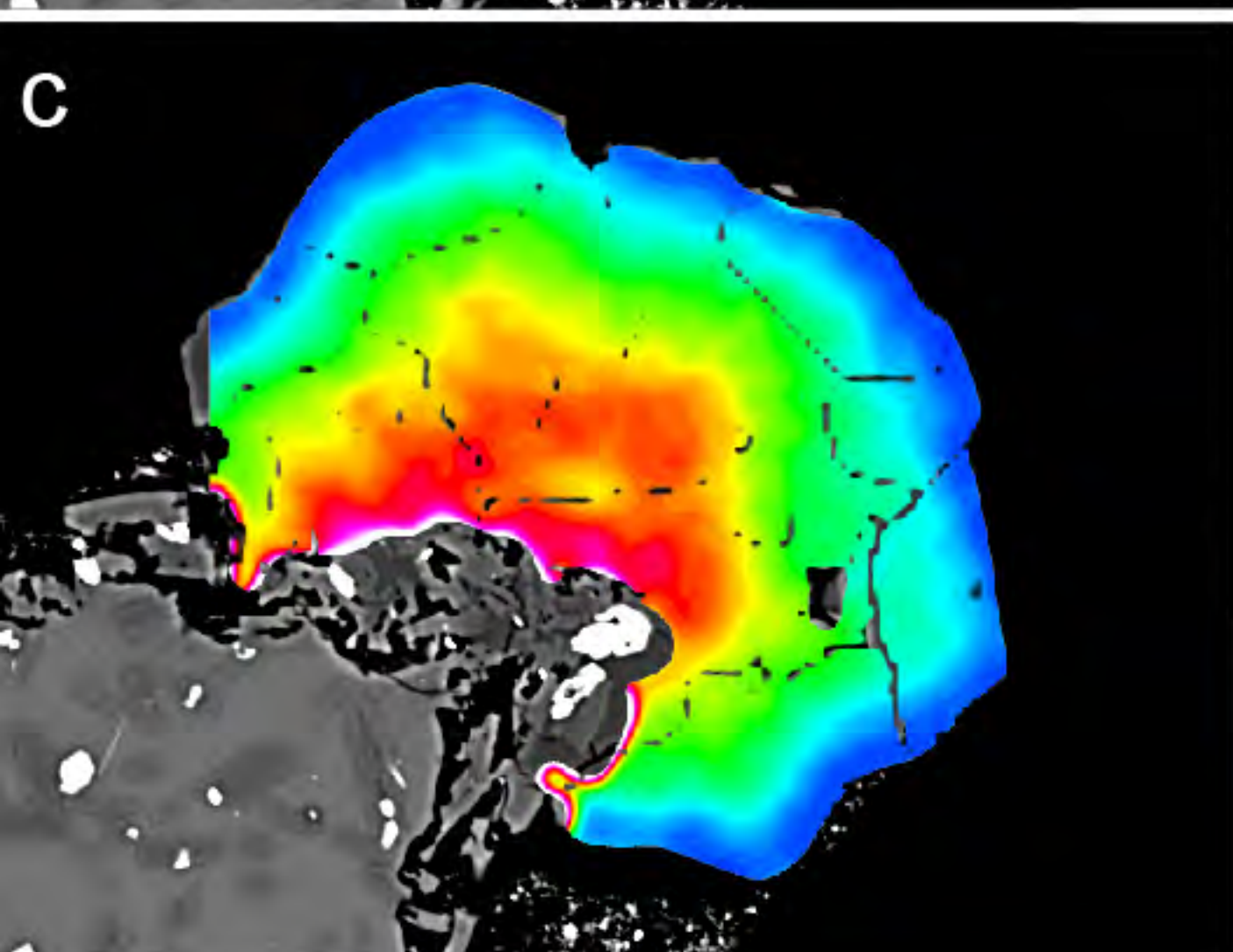
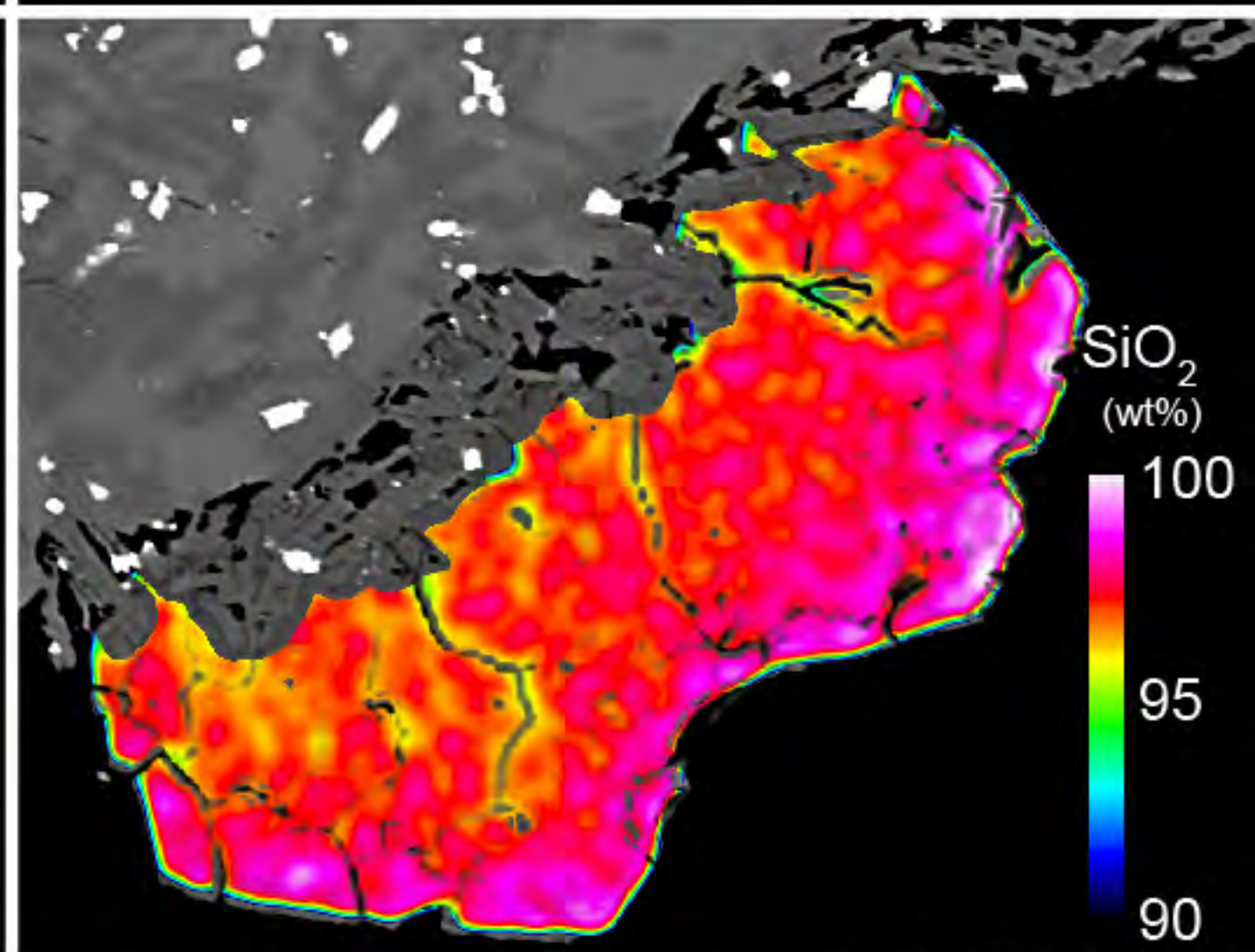
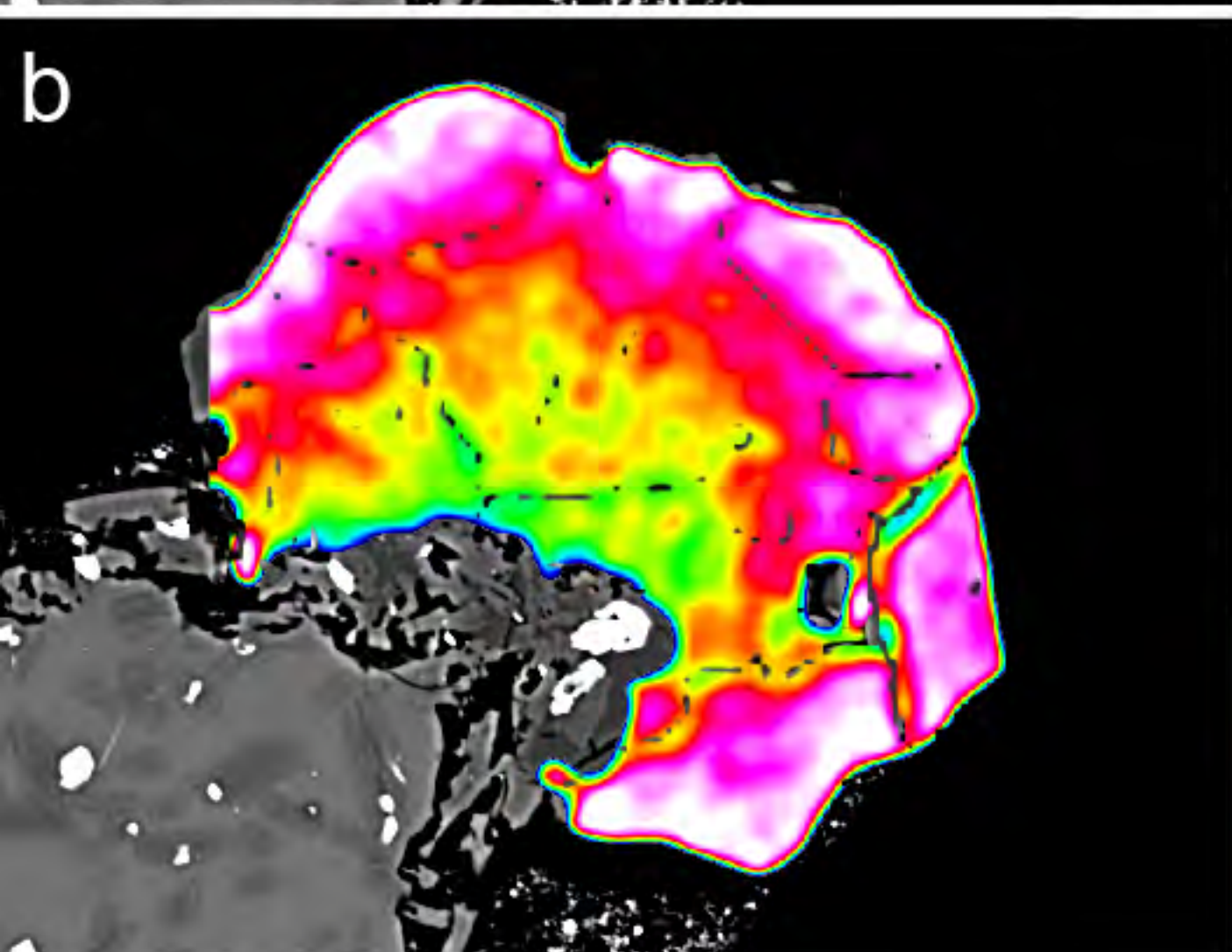
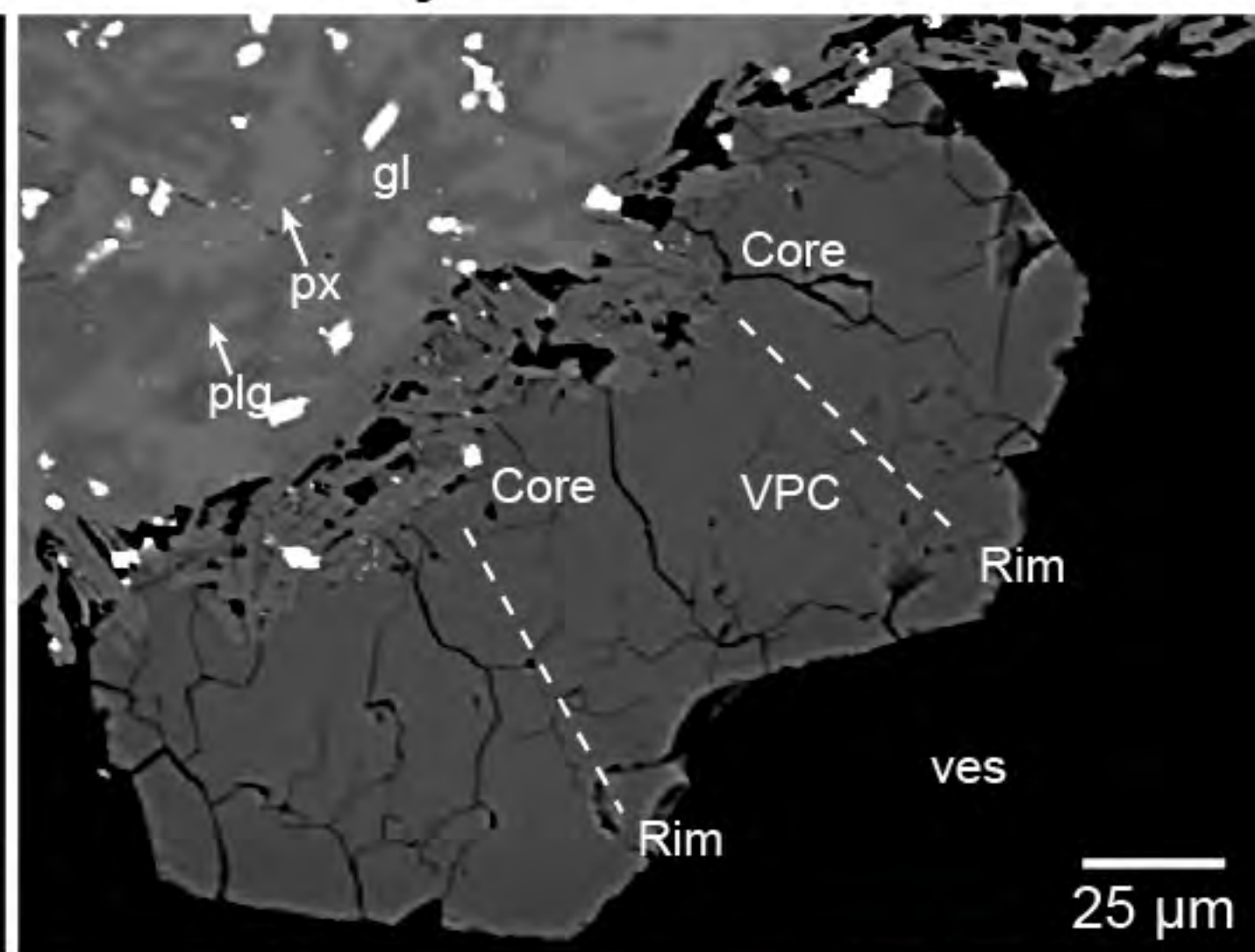
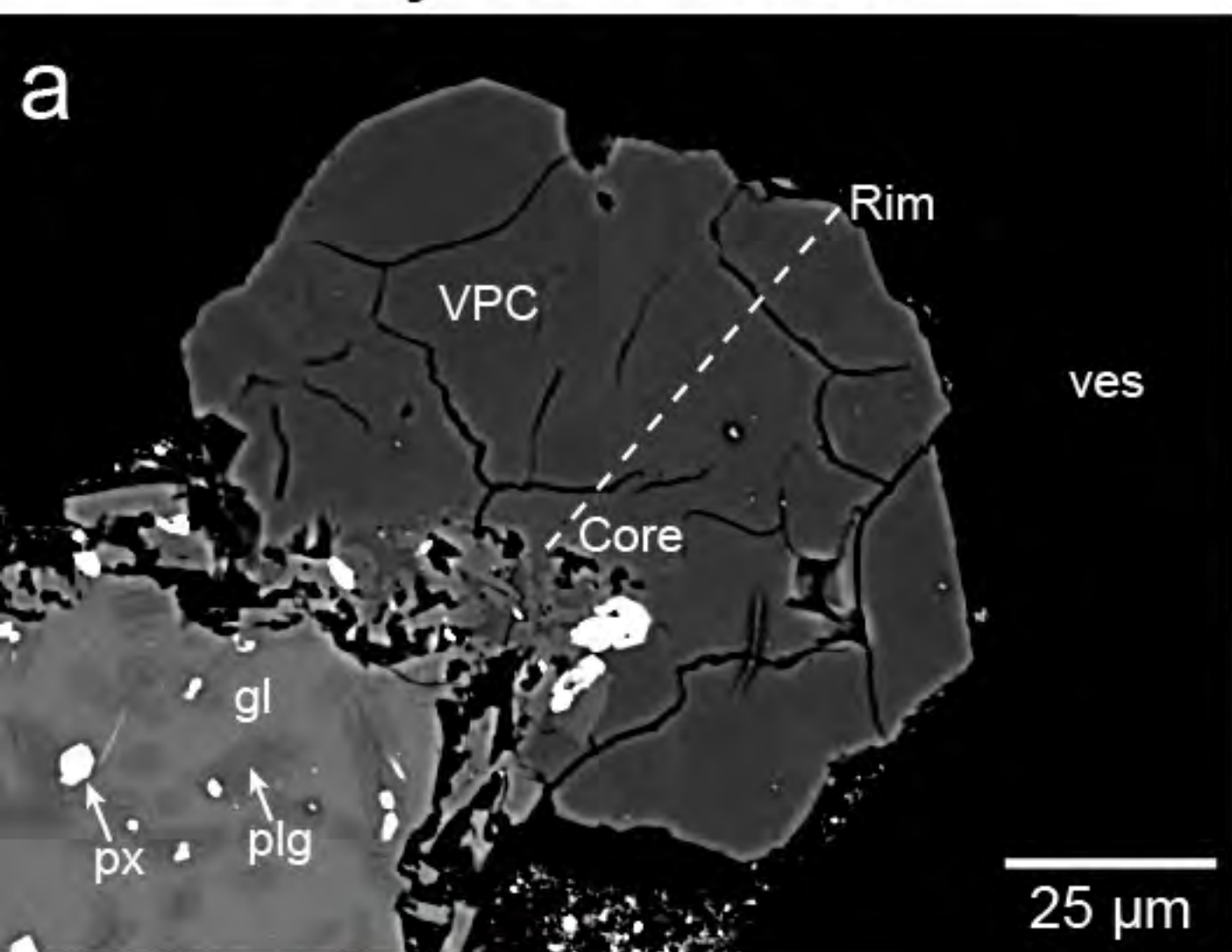


Figure 3

Crystal L10-01

Crystal L10-07

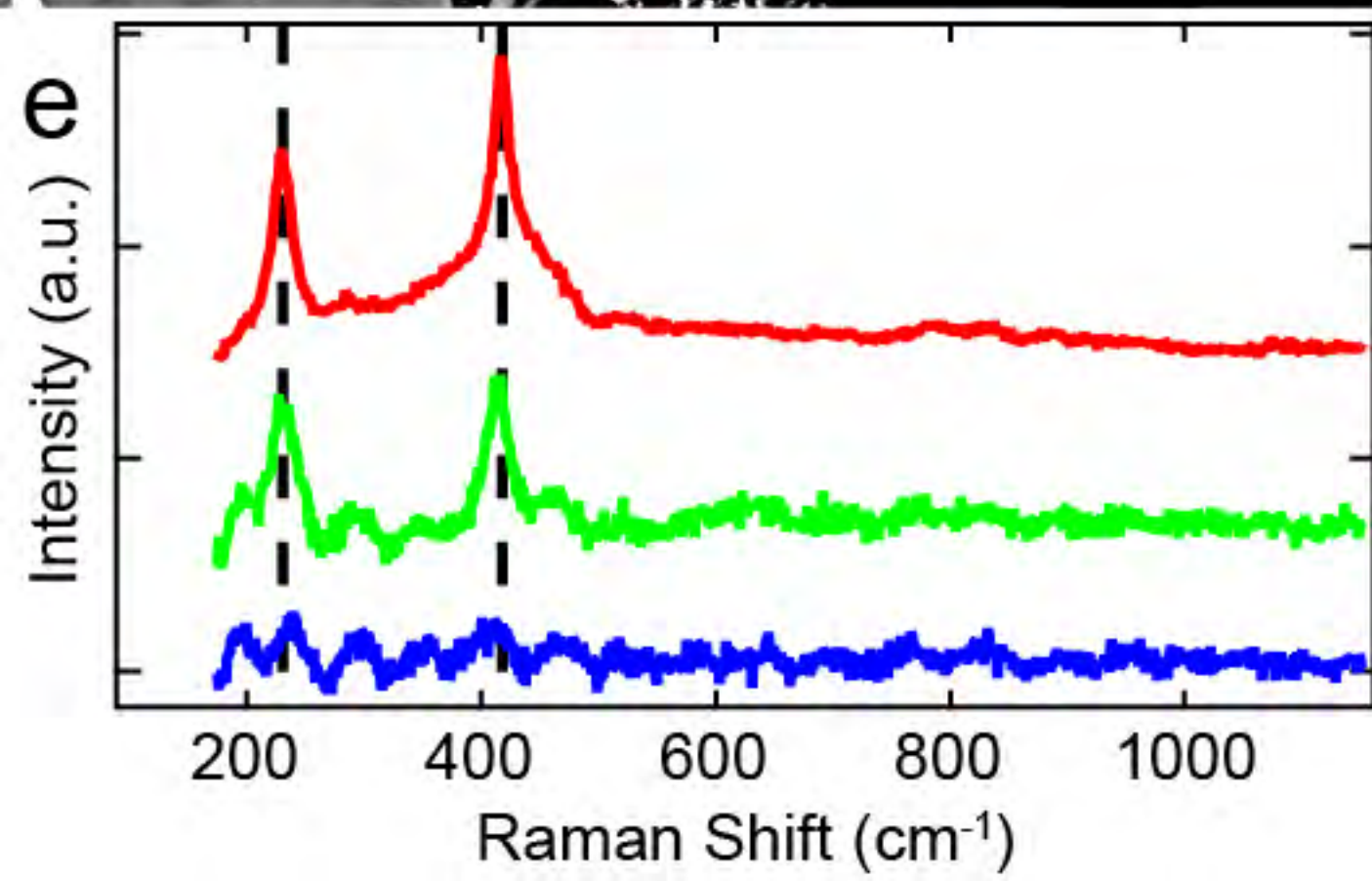
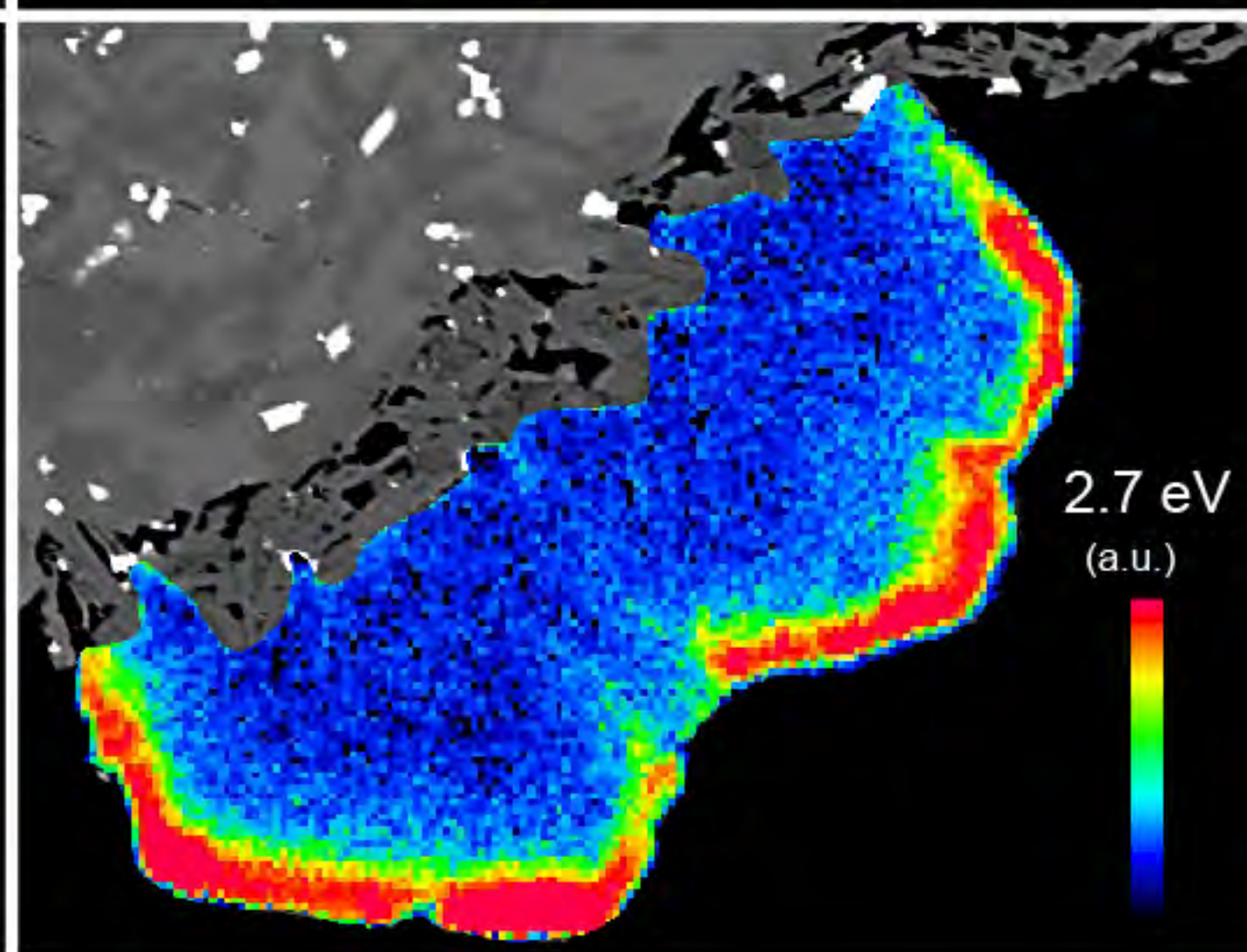
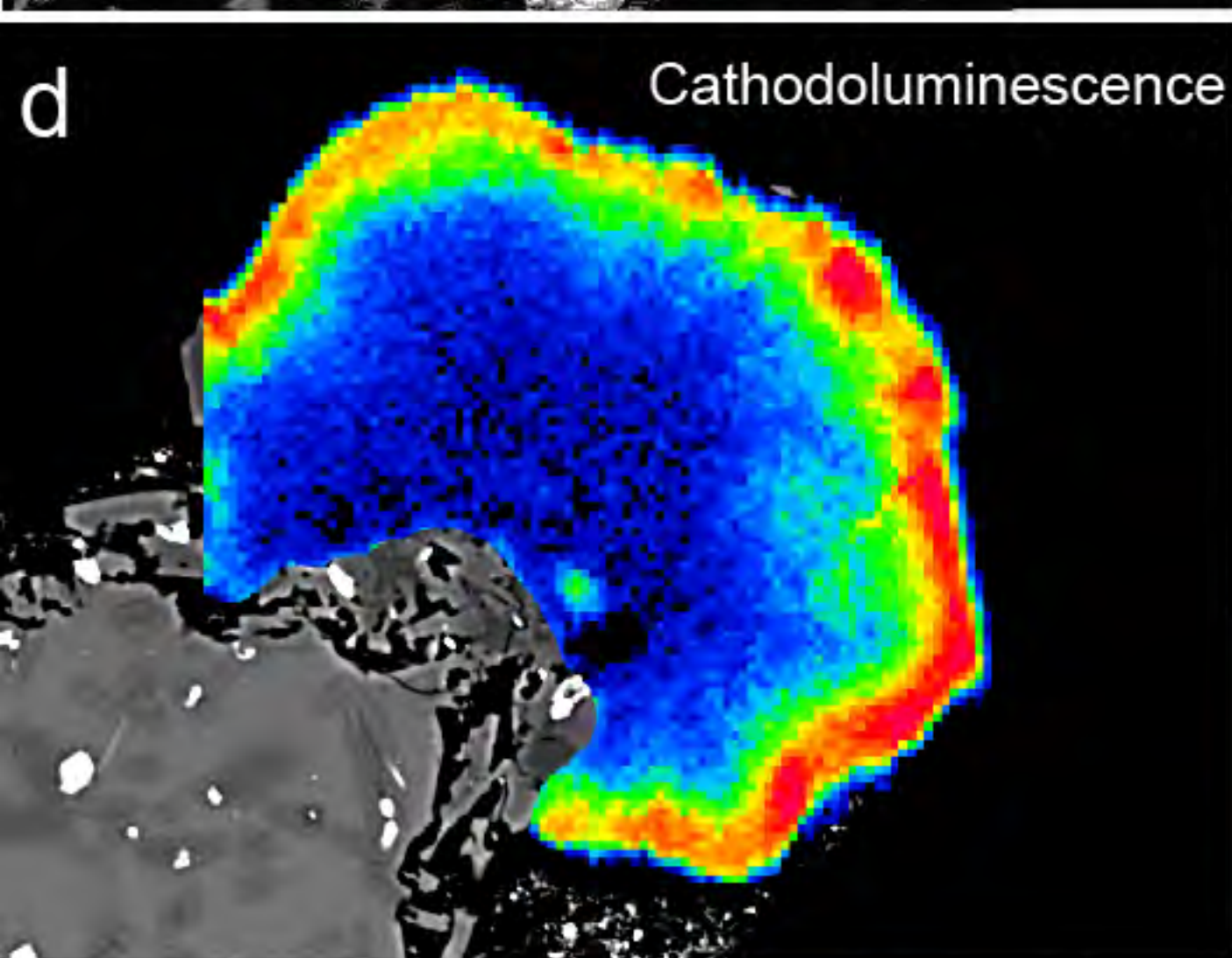
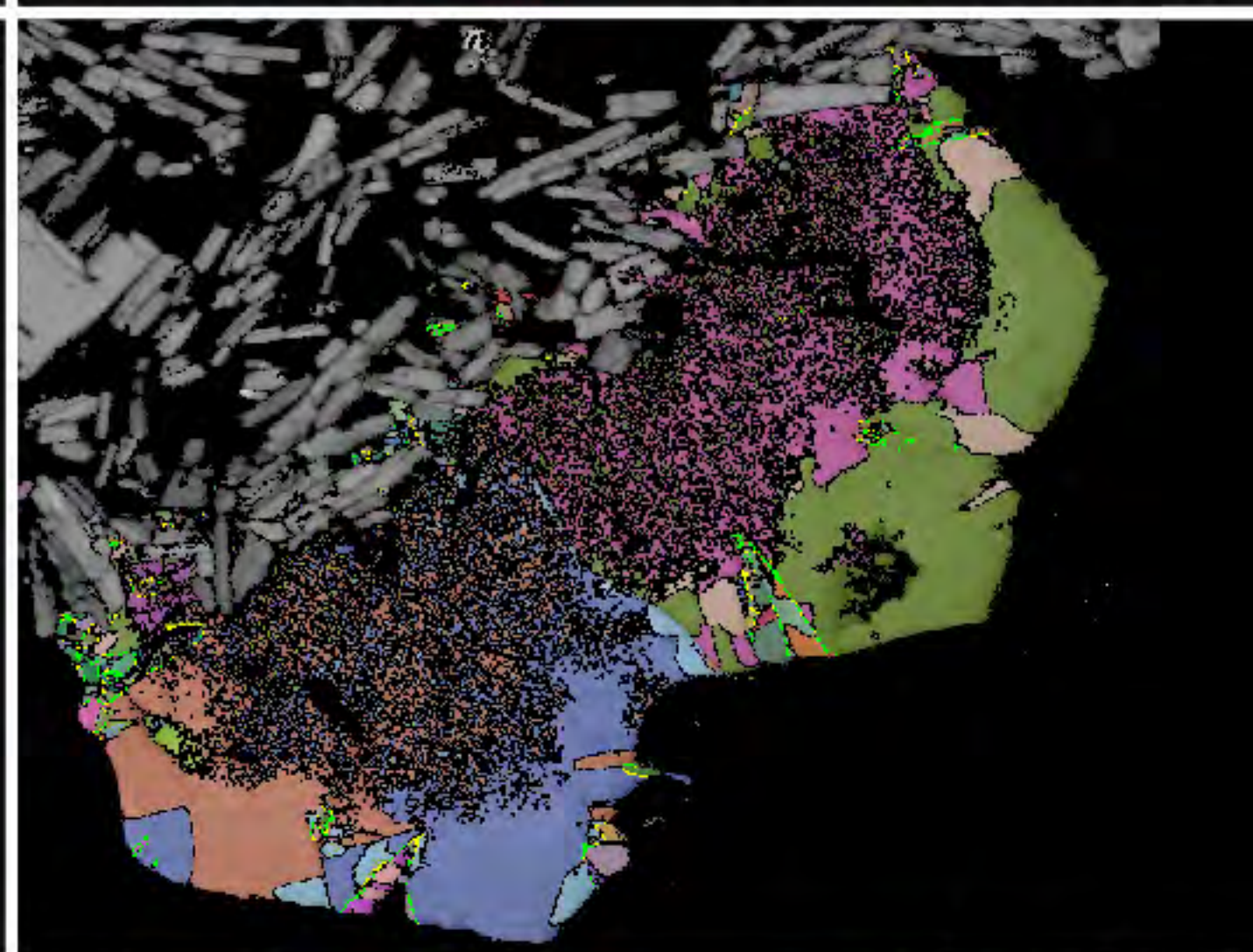
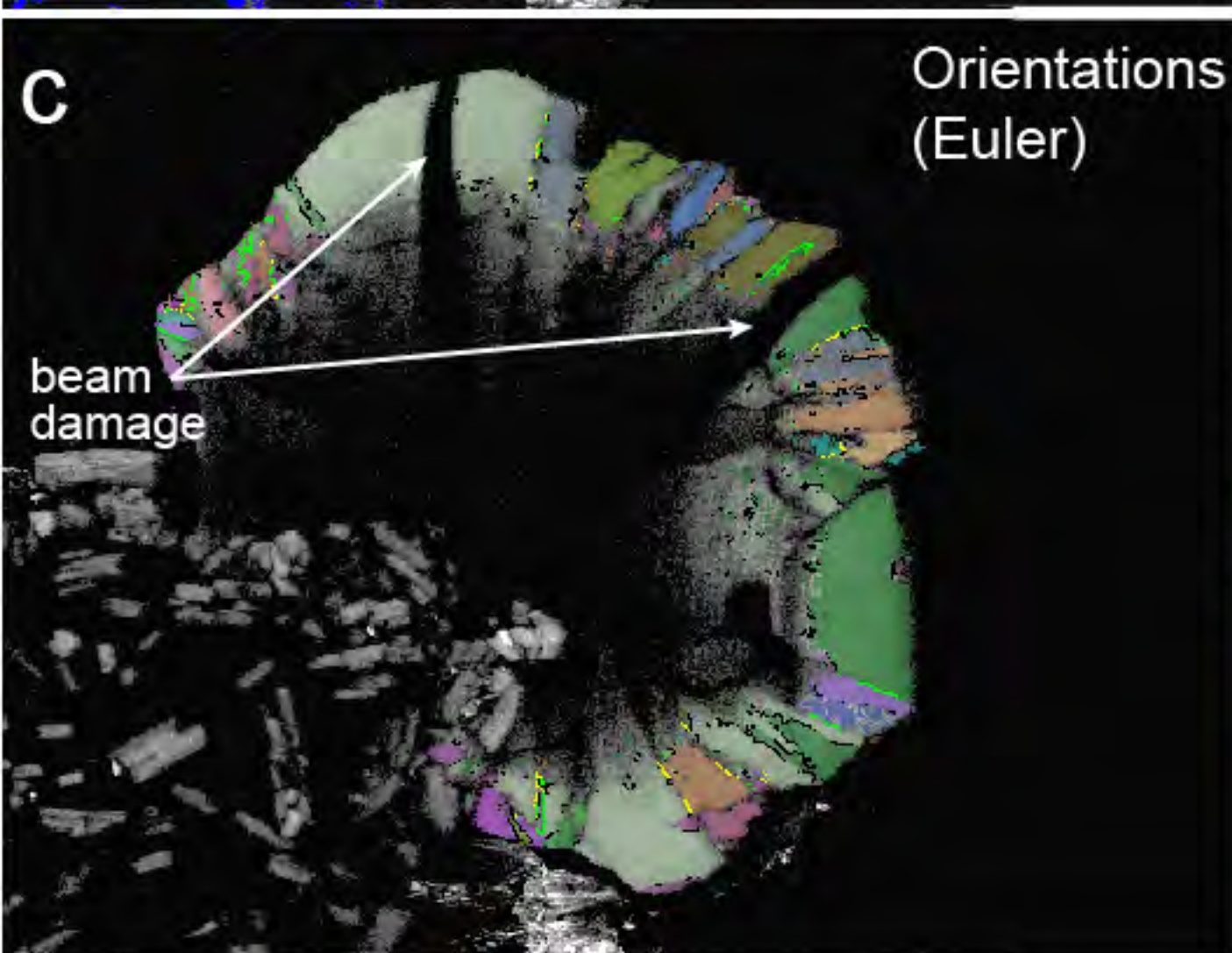
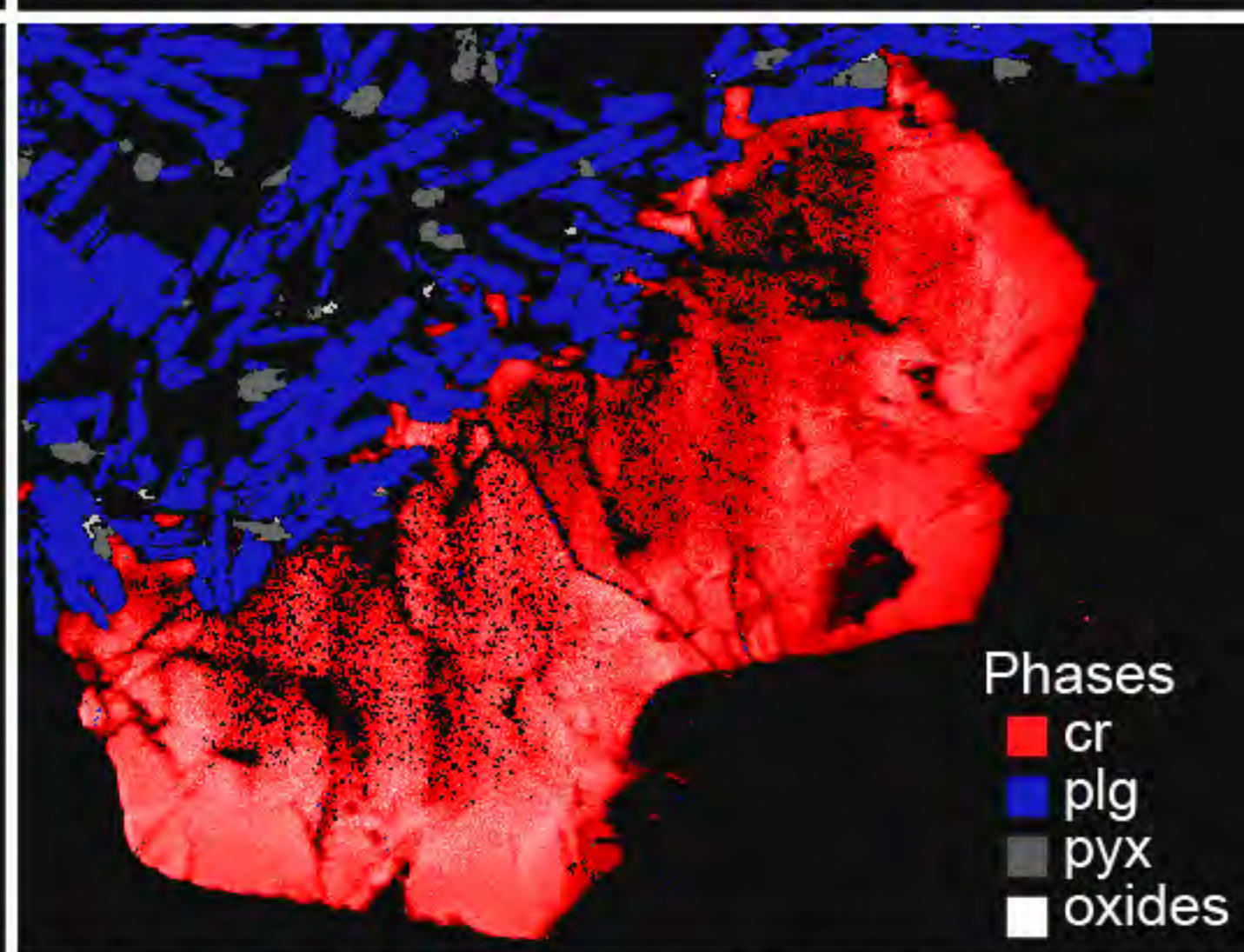
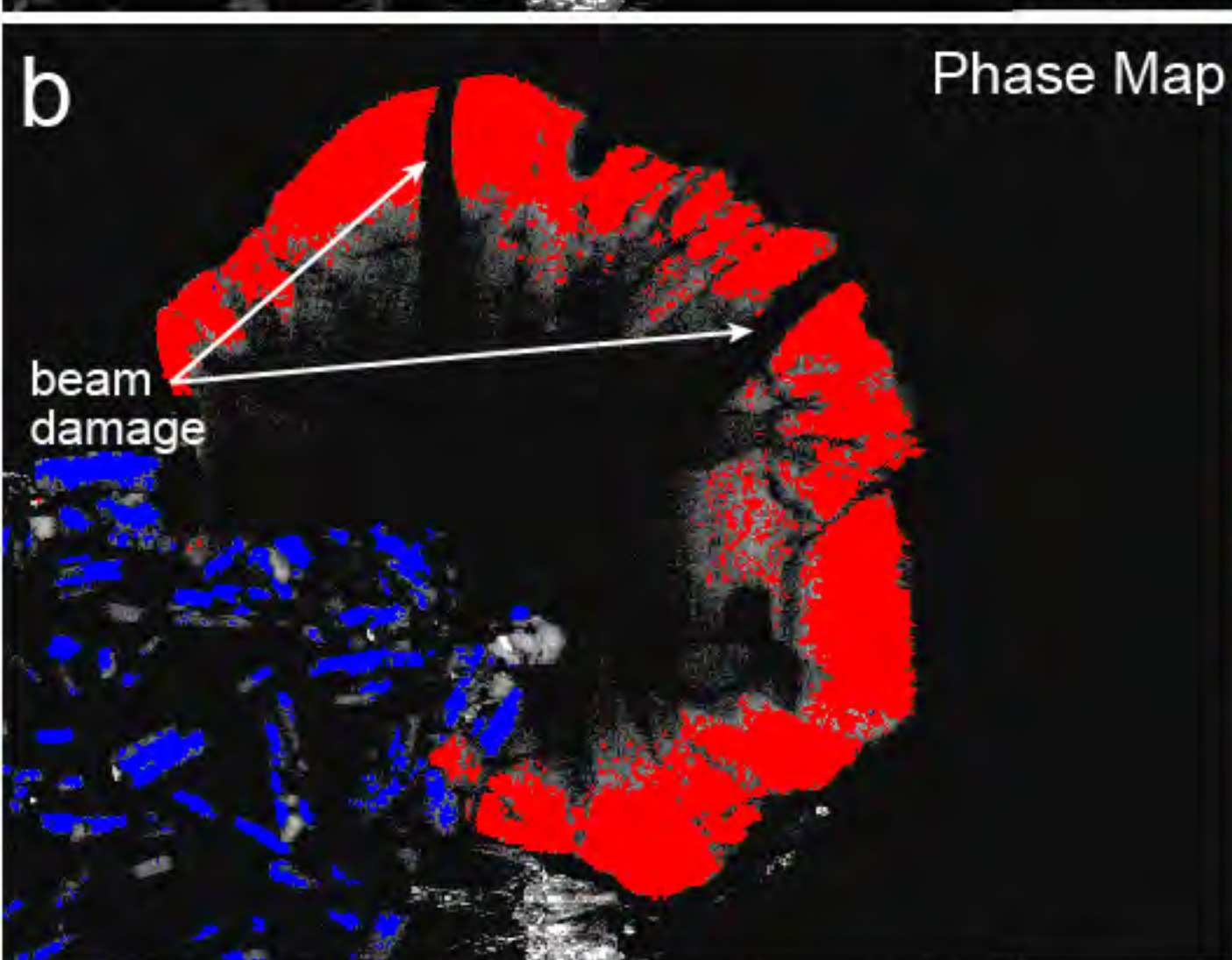
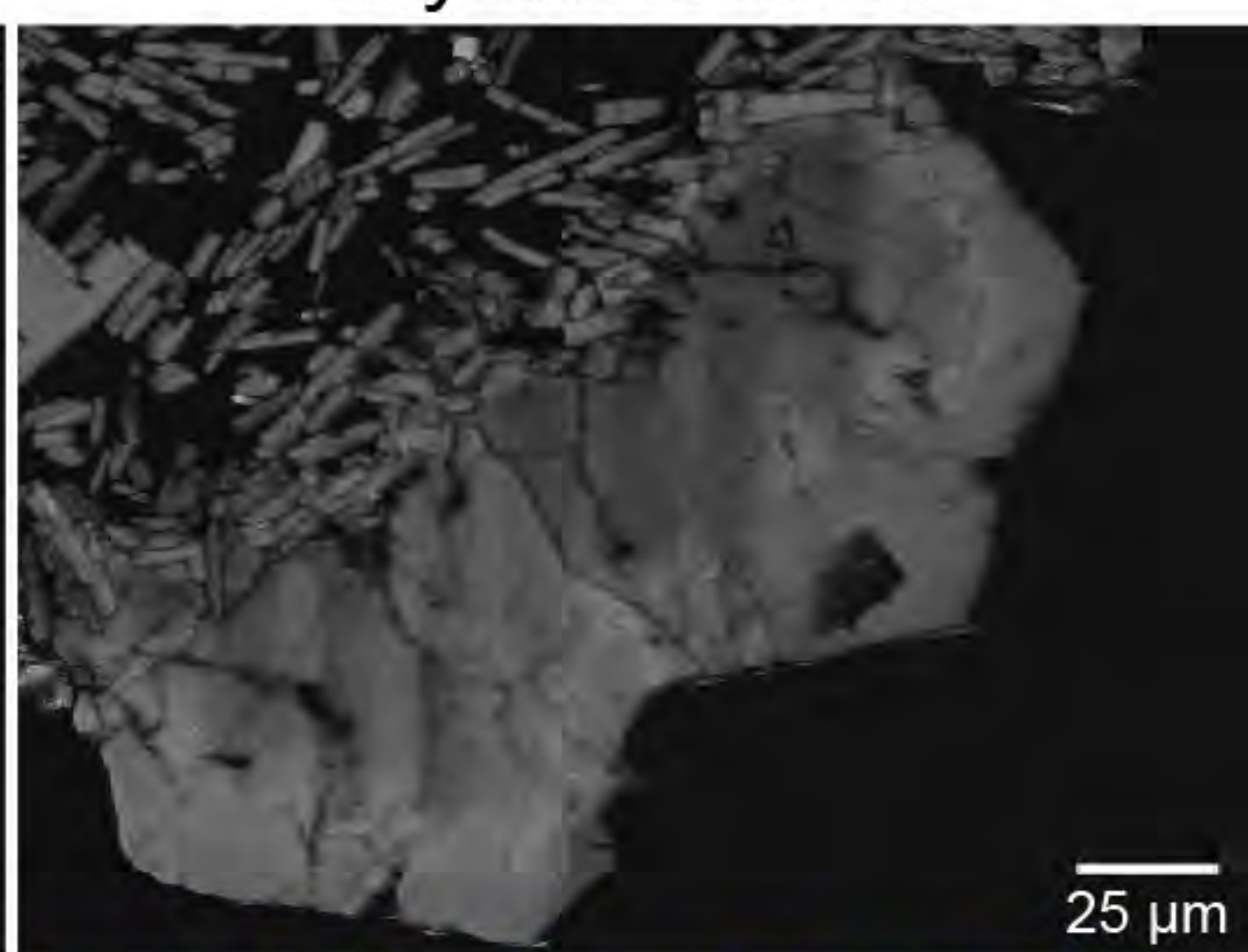
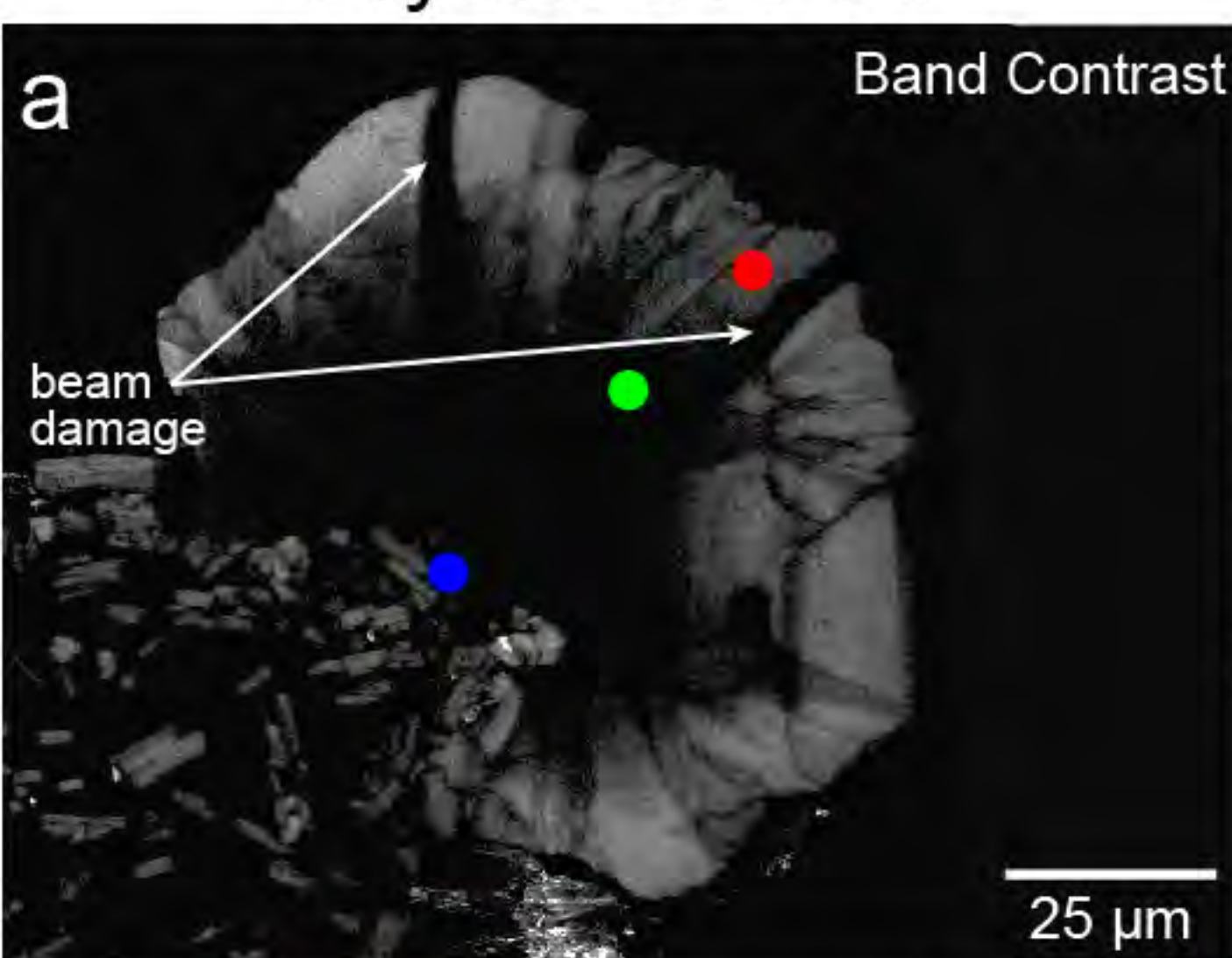


Figure 4

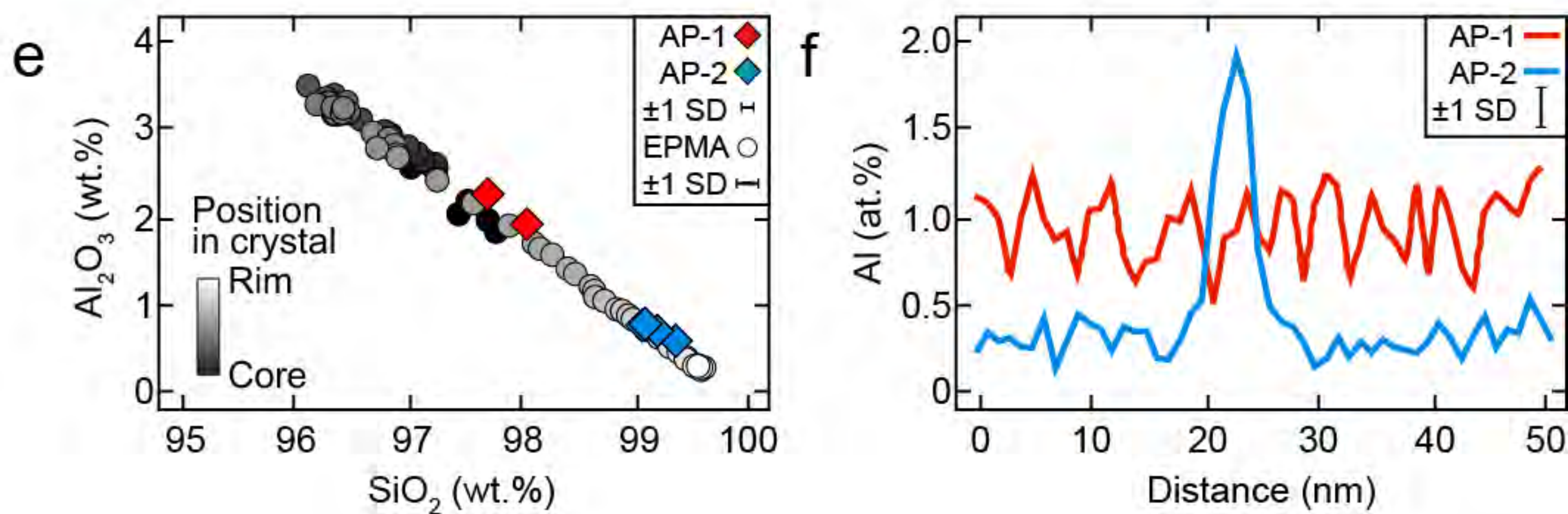
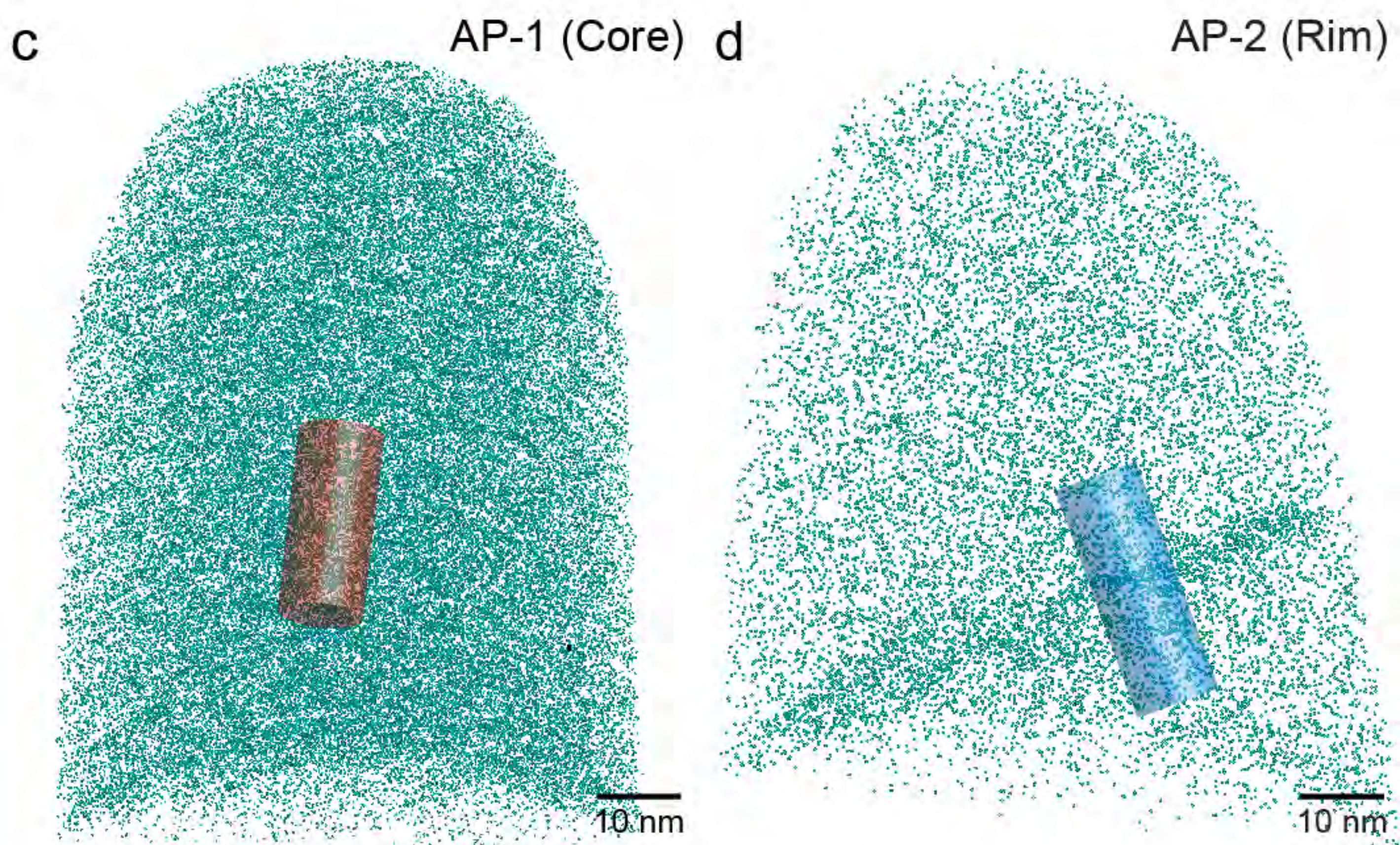
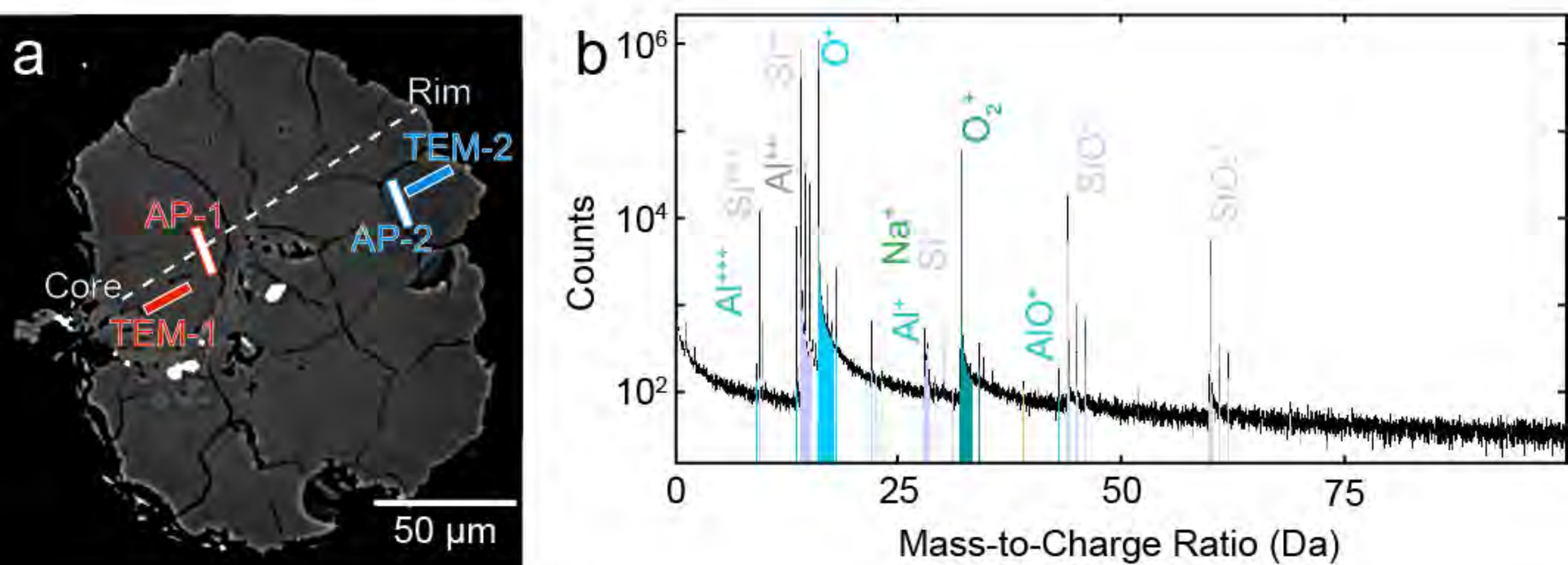


Figure 5

TEM-1 (Core)

TEM-2 (Rim)

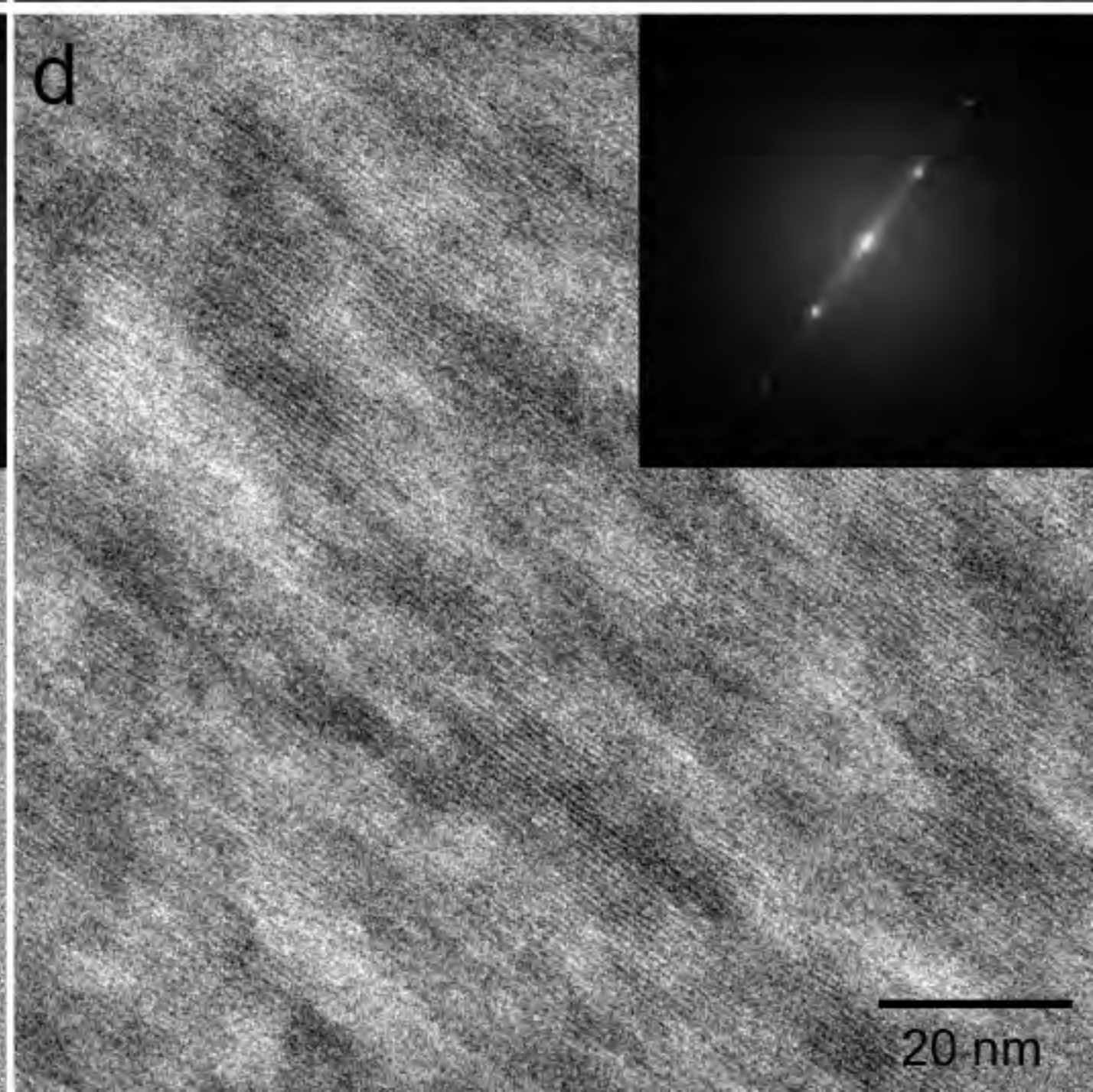
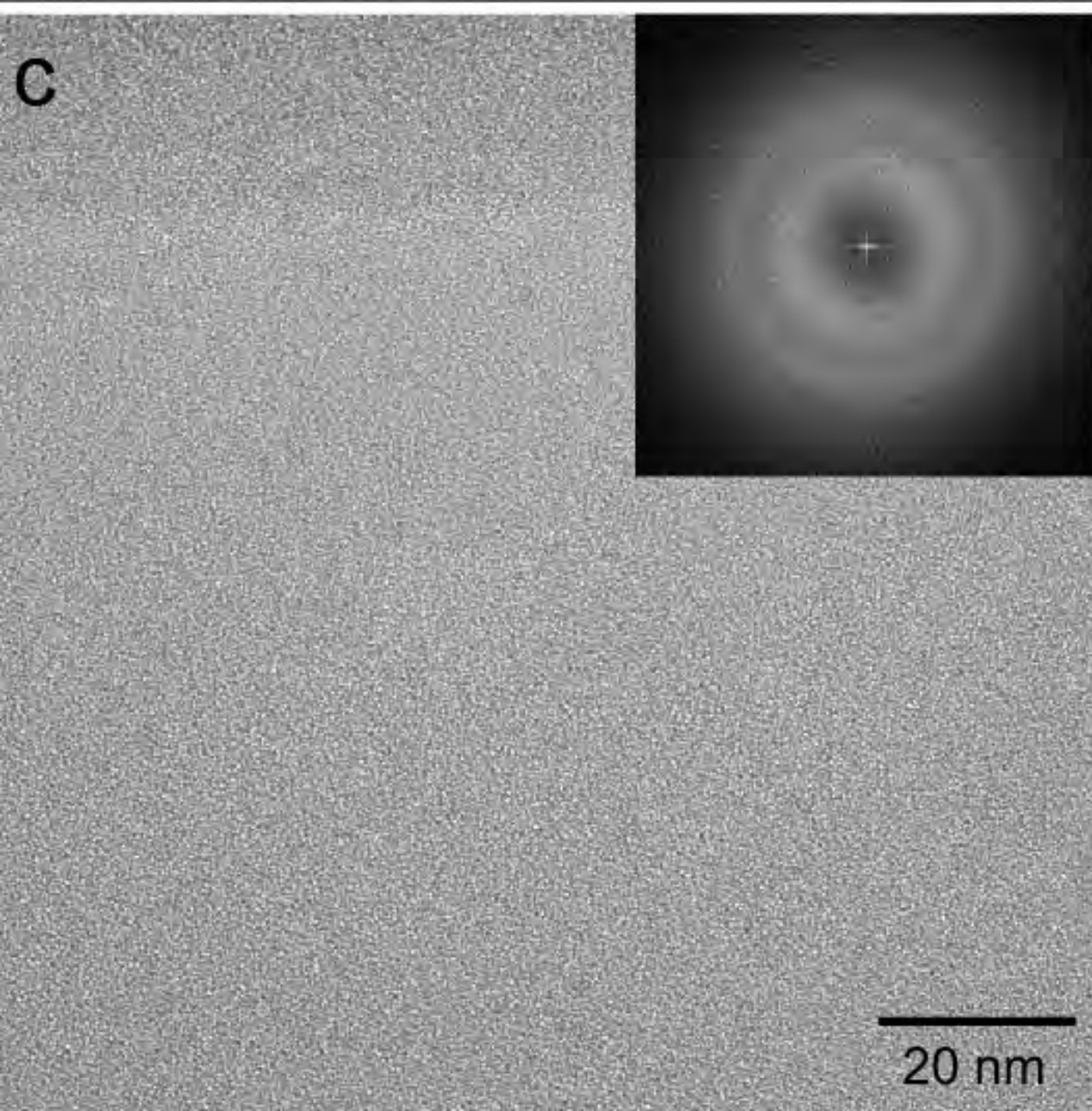
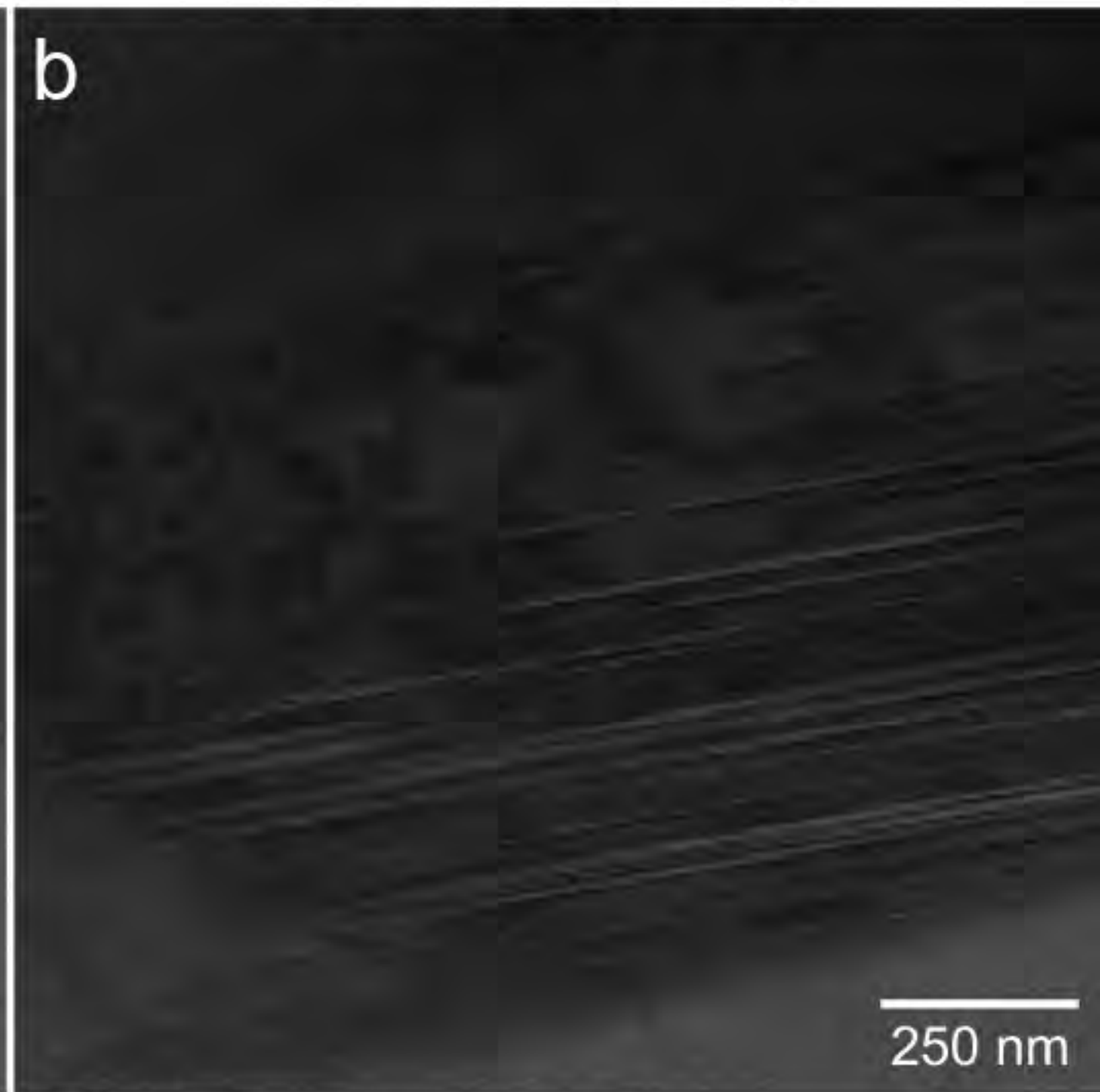
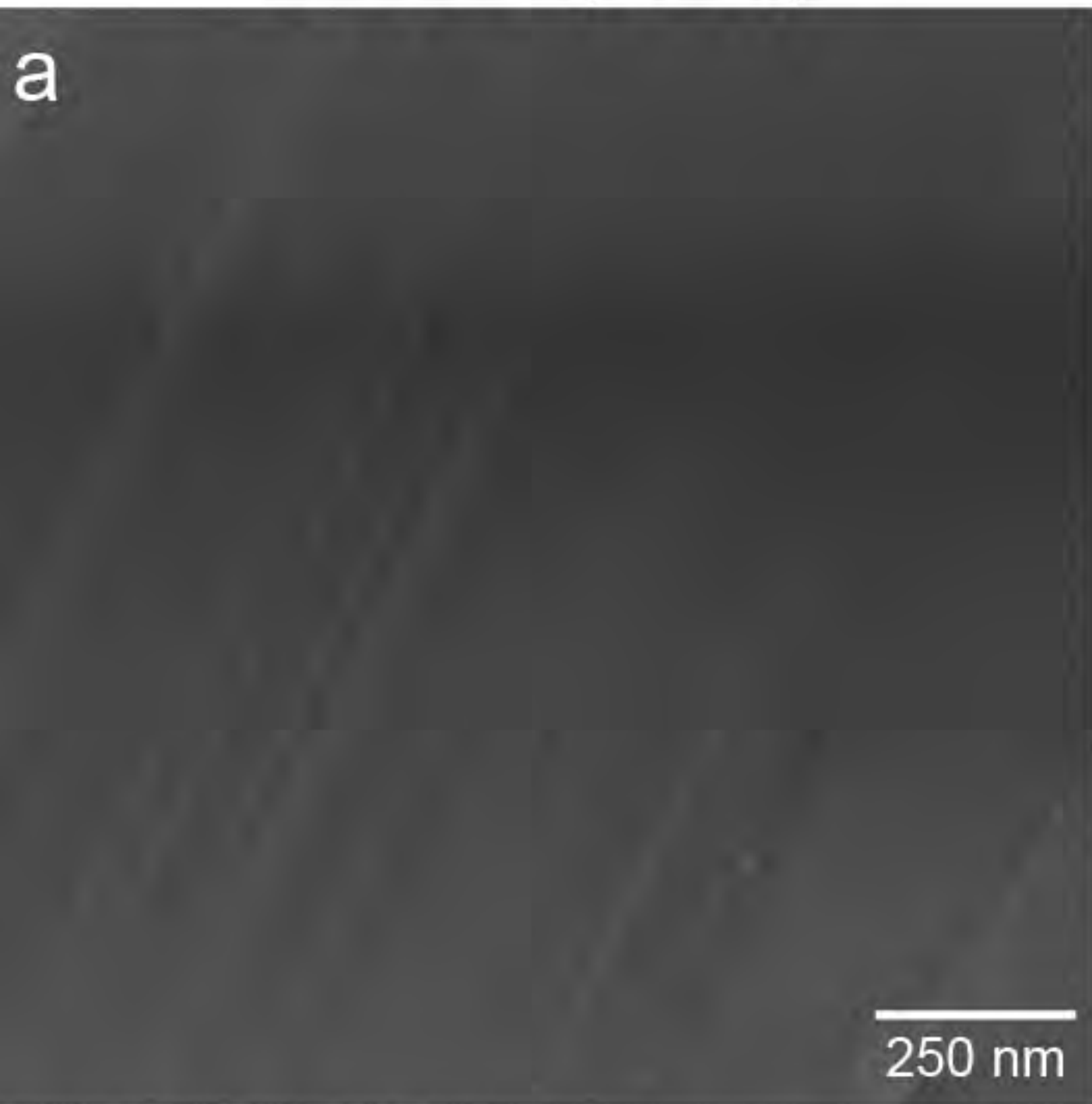


Figure 6

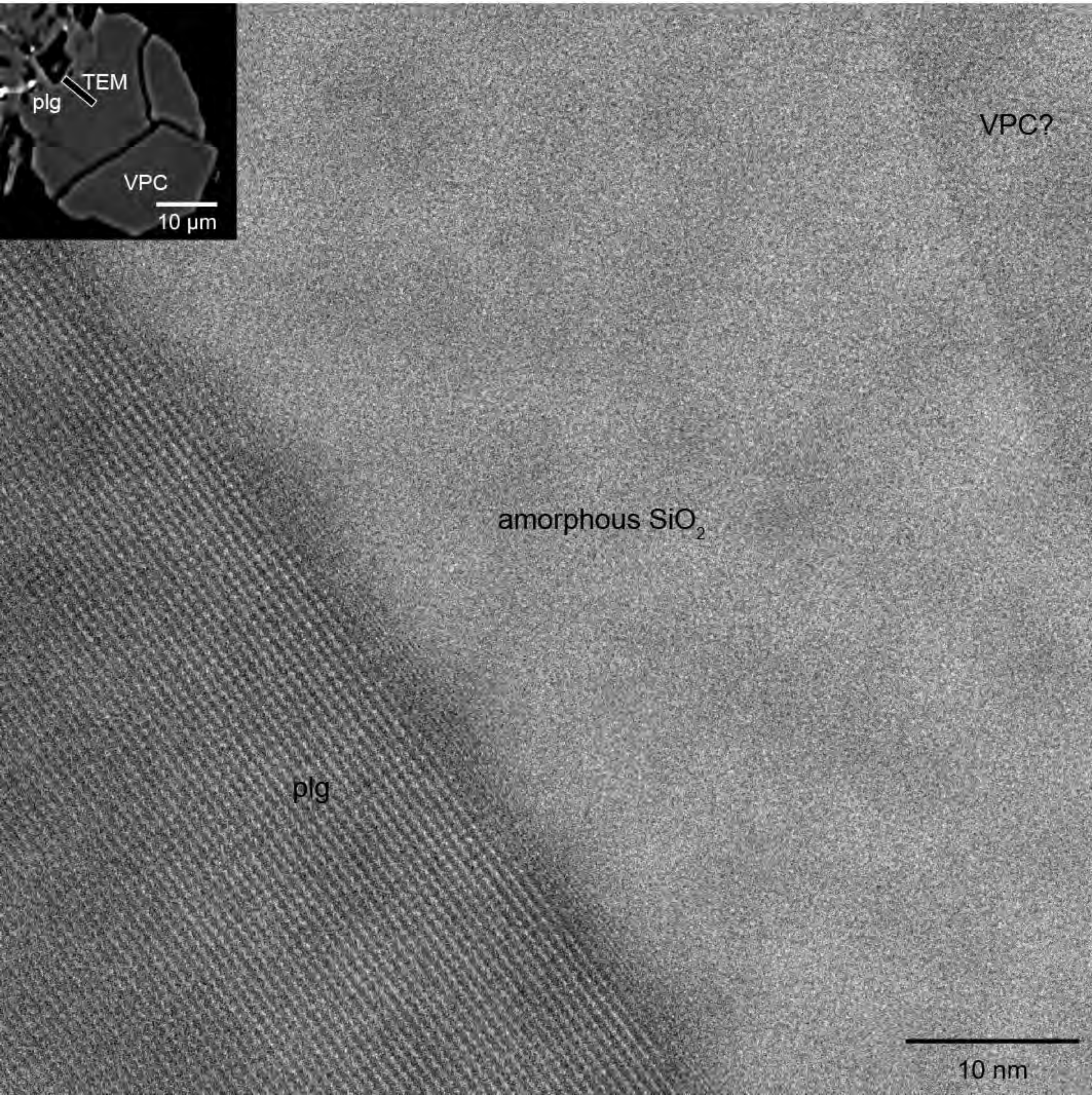
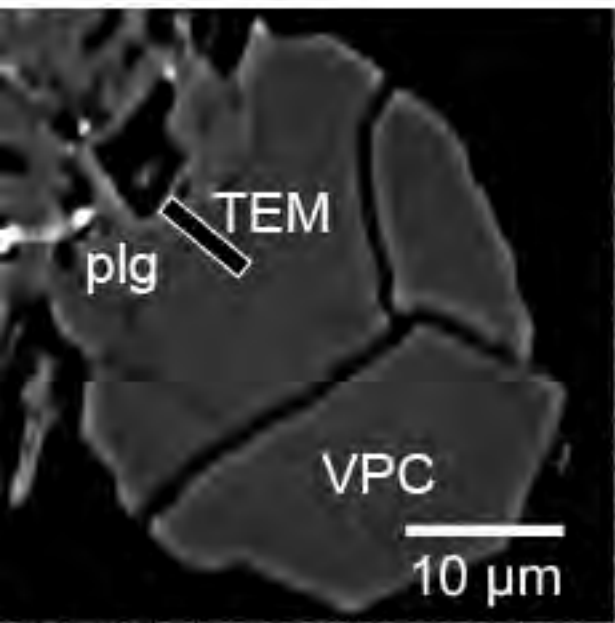


Figure 7

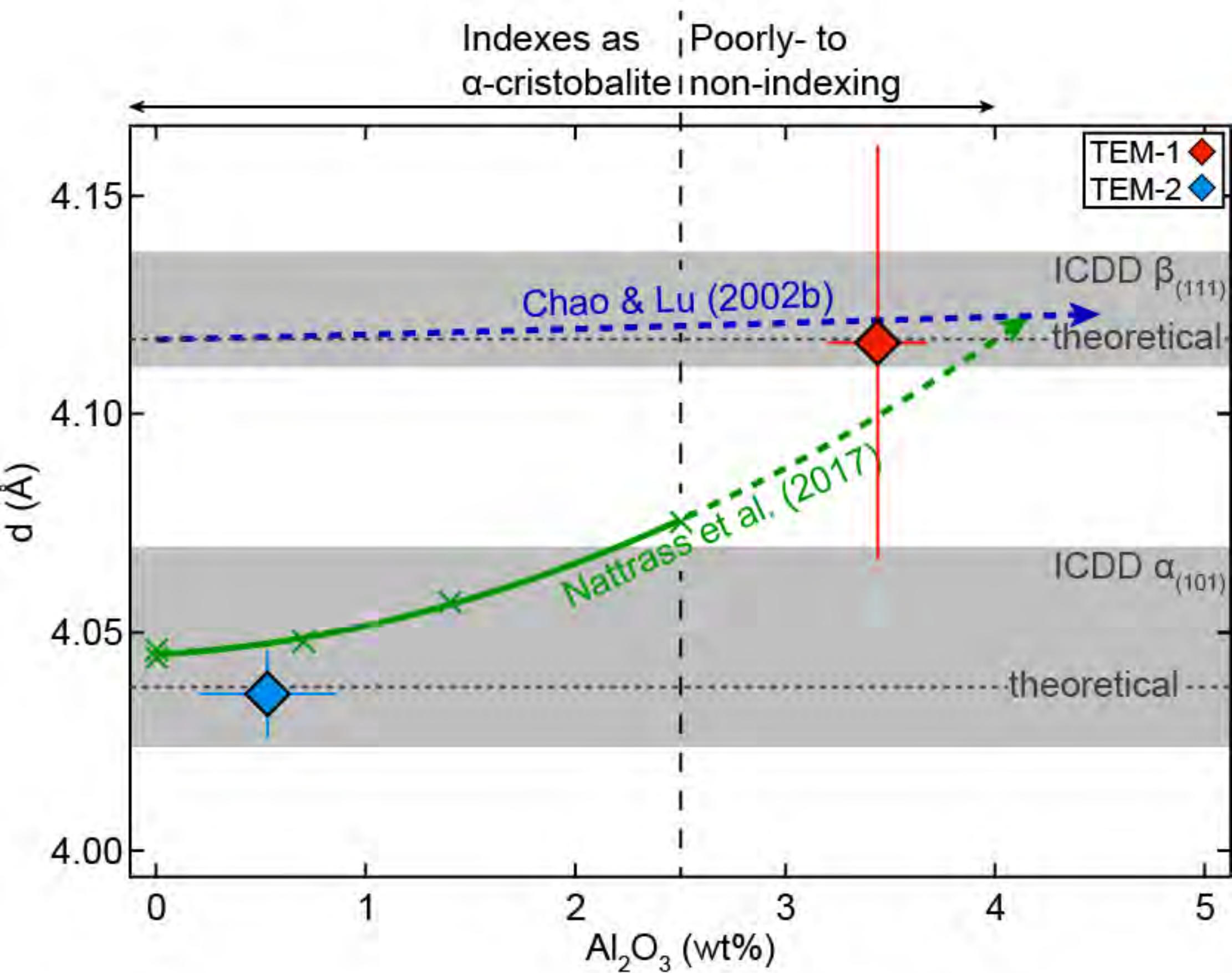


Figure 8

